Reliability analysis of fatigue crack growth in shallow shell structures using the Dual Boundary Element Method

Mengke Zhuang [a,*], Llewellyn Morse [b], Zahra Sharif Khodaei [a], M.H. Aliabadi [a]

[a] Department of Aeronautics, Imperial College London, South Kensington Campus, City and Guilds Building, Exhibition Road, SW7 2AZ, London, UK
[b] Department of Mechanical Engineering, University College London, Roberts Building, WC1E 6BT, London, UK

ARTICLE INFO

ABSTRACT

This work presents a novel methodology for fatigue life reliability analysis using a newly developed Dual Boundary Element Method-based Implicit Differentiation Method (DBEM-IDM) in shallow shell structures. The proposed DBEM formulations evaluate stress intensity factors and fatigue life sensitivities in shallow shells considering geometrical variables and curvature. The IDM formulations, obtained through direct differentiation of the shallow shell DBEM formulations, uses the First-Order Reliability Method (FORM) to assess the reliability index and probability of failure of shallow shell structures with multiple cracks. Two numerical examples were simulated to illustrate the effectiveness of the proposed methodology. The first example examines a shallow shell with a centre hole and cracks subjected to various loads. The critical crack length required to ensure structural reliability and inspectability is determined. Fatigue reliability assessment is performed for the same example, employing limit state functions expressed in terms of fatigue life. FORM results are compared with the results of Monte Carlo Simulations (MCS), and provided a maximum difference of 3.67%. Parametric analyses are conducted to identify significant variables that affect reliability, and it was found that precise determination of design parameters is necessary to reduce the probability of failure, particularly for the Paris law constants. The second example, featuring more complex geometry, involved assessing fatigue reliability in a cylindrical shallow shell structure with multiple cracks. The results of this example indicate a 3.49% maximum difference between FORM and MCS. The results exhibit a low error compared to the MCS, and the inherent efficiency of the IDM-based FORM underscores its suitability for addressing uncertainty in reliability analysis.

1. Introduction

In engineering problems, the existence of uncertainties is an inevitable problem. Traditionally, uncertainties have been managed in a deterministic manner by introducing safety factors to avoid catastrophic failure. However, this approach remains limited in its ability to provide insights into how individual parameters exert influence over the overarching system performance. In contrast, reliability analysis has emerged as a method tailored to address the stochastic characteristics of variables within the design process. This entails defining a performance criterion for a structure and offering the likelihood of successfully meeting this criterion [1]. Reliability analysis provides a framework to comprehend the impact of each parameter on the overall reliability of the structure, thereby enabling engineers to prioritize the most crucial factors during the design process.

The application of reliability techniques to structural problems has been conducted by the research community with a diverse array of methods. Notable examples include the application of reliability analysis to diverse domains such as nano-structures [2], corrosion in pipelines [3], and bimaterial cracked structures [4]. In the field of reliability analysis, methodologies can be broadly classified into two categories: direct and indirect methods. Direct methods, such as Monte Carlo Simulations (MCS) [5], have been widely utilized. MCS entails the exploration of possible uncertainties through extensive sampling. Furthermore, the fusion of such sampling techniques with meta-modelling methods [6] has significantly contributed to enhancing computational efficiency. Indirect techniques, such as the First-Order Reliability Method (FORM) and Second-Order Reliability Method (SORM) [7], approximate the limit state function, defining the boundary between success and failure, through first and second order Taylor expansions respectively. A critical aspect of FORM and SORM is the evaluation of the sensitivity of the limit state function to parameter variations. Commonly employed techniques for deriving

---

this sensitivity include the Finite Difference Method (FDM) and Implicit Differentiation Method (IDM). The FDM relies on finite differences to compute derivatives. Its precision is determined by the chosen step size, often requiring a convergence test to determine an optimal value for choosing the step size. Conversely, the IDM directly differentiates the limit state function, offering an enhancement in computational efficiency over the FDM [8].

To enhance computational efficiency, this study employs the Dual Boundary Element Method (DBEM) coupled with the Crack Surface Displacement Extrapolation (CSDE) technique, to assess the sensitivity of crack tip stress intensity factors with respect to changes in design parameters. The DBEM, an effective alternative to the Finite Element Method (FEM) and Virtual Element Method (VEM) [9,10] for crack problems, only requires the modelling of the outer boundary of the structure, with cracks treated as additional boundaries, facilitating automatic crack advancement without the need for re-meshing. Such an approach substantially reduces computational overhead, particularly evident in fatigue crack growth analyses. The formulation of the Boundary Element Method (BEM) can be categorized into two distinct approaches. The first is the direct BEM formulation, wherein the system of equations primarily involves unknowns related to displacement and traction fields. The second approach is the indirect BEM formulation, which is formulated based on the fictitious fluxes. This latter formulation was initially developed by Crouch [11,12], and its application to crack problems using the displacement discontinuity method has been detailed in [13,14]. This study, however, is predominantly focused on the direct BEM formulation, examining its application and effectiveness in addressing the crack-related problem in shallow shell structures. A comprehensive introduction to the DBEM formulation and stress intensity factor evaluation can be found in [15].

Shallow shell problems are an important subject in engineering design processes, owing to the widespread use of shallow shells in aircraft and naval structures due to their favourable attributes of low weight and high strength. The shallow shell formulations of the DBEM were first developed based on the 2D BEM formulation proposed by Portela [16]. Based on this work, an advancement was made by Dirgantara and Aliabadi [17,18] for bending problems in shallow shell structures, drawing from the classic theory [19] and Reissner's theory for thin elastic shells [20], which considered transverse normal stress and transverse shear deformation. Reissner's plate theory was pivotal in deriving the fundamental solutions, with the Dual Reciprocity Method (DRM) [21] employed to transfer the domain integrals to boundary integrals. This approach has found applications across various works, such as the analysis of assembled plate structures [22], addressing buckling concerns in shallow shells [23], and the study of composite shallow shell structures [24]. Additionally, fatigue assessments have been conducted, encompassing problems such as crack propagation in cortical bone [25], the analysis of pressurized shells [26], and dynamic fracture assessments in plates [27,28]. In this work, the methodology proposed in [17] is employed to evaluate stress intensity factors and their sensitivities with respect to the design parameters of a shallow shell structure subjected to combining tension, bending and uniform pressure load.

The majority of indirect approaches to reliability analysis in the existing literature have predominantly favoured the FEM [29–31]. However, little attention has been paid to the application of the shallow shell DBEM in reliability analysis. The studies conducted by [8,32] included employing the Boundary Element Method (BEM) on a 2D structure, incorporating uncertainties related to geometry and material properties. Within these contexts, the limit state function, expressed in terms of maximum stress within the structure was used in both the FORM and the SORM. Similar work has been conducted in [33], where BEM was incorporated with FORM, and the results were compared against MCS. Notably, the implications of the coefficient of variance (COV) embedded within the design parameters were considered. Further works with the application of BEM include a modified version

of BEM, the Spline Fictitious Boundary Element Method (SFBEM), which was employed to conduct reliability analysis on a Reissner plate bending problem [34] with the definition of the failure state based on a threshold bending moment within the structure.

Fatigue is of high interest in the field of structural design. The evaluation of stress intensity factors (SIFs) and the variations in design parameters stand as an important subject in the domain of failure analysis. Numerous studies have emerged in the field of reliability analysis concerning cracked structures. Several notable works can be found. For instance, in the work presented by [35], a plate subjected to the combined effects of bending, tension, and domain load, and featuring a centrally situated slant crack, was meticulously simulated using the DBEM. Both the IDM and the FDM were employed to examine the sensitivity of crack front SIFs. Furthermore, the fatigue reliability assessment was proposed in [36], where the durability of a railway steel component was assessed to determine its design service life. Additionally, a novel approach for sensitivity evaluation was proposed in [37], involving derivatives with respect to the local coordinate system to accurately account for directional changes during crack propagation. Similar work can be found in [38], where the consideration extends to structures bearing multiple cracks.

Despite the existing research in this domain, a study on the application of the DBEM to fatigue reliability analysis for shallow shell problems has not yet been conducted. This study aims to extend the work initiated by Morse [35] and Huang [37] to formulate a DBEM-based IDM specific to cracked shallow shell problems, thereby enabling an accurate assessment of SIF sensitivities. Within this framework, a fatigue reliability assessment is conducted with the FORM, accounting for the uncertainties inherent in fatigue crack growth. The outcomes from this fatigue reliability assessment hold the potential to contribute to determining a structure's service life or identifying a suitable inspection interval in real-world engineering scenarios.

The paper's structure unfolds as follows: Section 2 outlines the methodology encompassing DBEM formulations and their associated derivatives. In addition, a brief introduction of the FORM is given. In Section 3.1, a numerical case study is presented, featuring a shell structure with two cracks and a central hole in the reliability analysis. The results of the reliability analysis are presented. A second numerical example in Section 3.2 involving more complex geometry was used for fatigue life reliability assessment to further illustrate possible practical applications of the DBEM-IDM formulations. A comparison of results obtained from FORM and MCS is provided. Further elaboration on the formulation of stress intensity factor derivatives can be found in Appendix.

2. Methodology

This section introduces the formulation of the Dual Boundary Element Method (DBEM) and the Implicit Differentiation Method (IDM) for shallow shell structures, encompassing the assessment of Stress Intensity Factors (SIFs) and their derivatives. Additionally, a brief overview of reliability analysis using the Most-Probable Point (MPP) method is provided.

2.1. DBEM for shallow shell structures

This section introduces the DBEM formulations developed for shallow shell structures, building upon the work by [17,18]. Derivatives of boundary integral equations, fundamental solutions, and particular solutions for the DRM technique were outlined in a previous study by [39]; hence, this paper focuses solely on the DBEM formulations. Latin letter indices (e.g., i, j, k) range from 1 to 3, while Greek letter indices (e.g., α, β) span from 1 to 2.
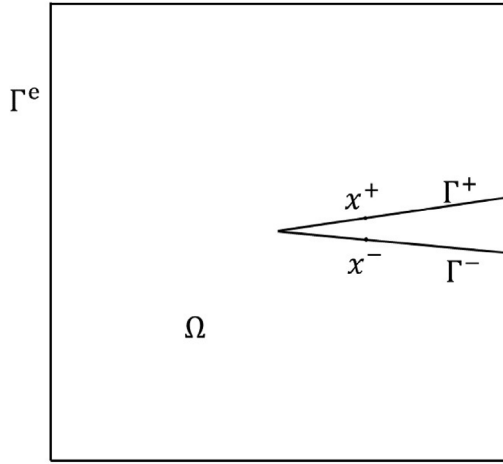
Fig. 1. A structure containing upper and lower crack surfaces labelled as Γ^+ and Γ^-. The structure's overall boundary is composed of $\Gamma = \Gamma^e + \Gamma^+ + \Gamma^-$, where Γ^e represents the outer boundary. The enclosed domain within this boundary is designated as Ω. The source points corresponding to the upper and lower crack surfaces are denoted as x^+ and x^-, respectively.

Consider a structure featuring a crack with upper and lower crack surfaces as shown in Fig. 1, characterized by principal curvatures $\kappa_{11} = 1/R_1$ and $\kappa_{22} = 1/R_2$, where R_1 and R_2 represent the radius of curvature of the shell in the x_1 and x_2 directions, respectively. In DBEM, the crack surfaces are modelled as two coinciding surfaces: the collocation on the point on the upper surface (x^+) is governed by displacement integral equations, and the lower surface point (x^-) is governed by traction integral equations.

The displacement integral equations for the upper surface are:

$$
\frac{1}{2}w_j\left(x^+\right) + \frac{1}{2}w_j\left(x^-\right) + \fint_\Gamma P_{ij}^*\left(x^+,x\right) w_j(x)d\Gamma(x)
$$
$$
= \int_\Gamma W_{ij}^*\left(x^+,x\right) p_j(x)d\Gamma(x)
$$
$$
- \int_\Omega W_{i3}^*\left(x^+,X\right) \kappa_{\alpha\beta} B\frac{1-\nu}{2}\left[u_{\alpha,\beta}(X) + u_{\beta,\alpha}(X)\right.
$$
$$
\left.+ \frac{2\nu}{1-\nu}u_{\phi,\phi}(X)\delta_{\alpha\beta}\right] d\Omega(X) \tag{1}
$$
$$
- \int_\Omega W_{i3}^*\left(x^+,X\right) \kappa_{\alpha\beta} B\left((1-\nu)\kappa_{\alpha\beta} + \nu\delta_{\alpha\beta}\kappa_{\phi\phi}\right) w_3(X)d\Omega(X)
$$
$$
+ \int_\Omega W_{i3}^*\left(x^+,X\right) q_3(X)d\Omega(X)
$$

and

$$
\frac{1}{2}u_\alpha\left(x^+\right) + \frac{1}{2}u_\alpha\left(x^-\right) + \fint_\Gamma T_{\theta\alpha}^*\left(x^+,x\right) u_\alpha(x)d\Gamma(x)
$$
$$
+ \int_\Gamma U_{\theta\alpha}^*\left(x^+,x\right) B\left[\kappa_{\alpha\beta}(1-\nu) + \nu\delta_{\alpha\beta}\kappa_{\phi\phi}\right] w_3(x)n_\beta(x)d\Gamma(x)
$$
$$
- \int_\Omega U_{\theta\alpha}^*\left(x^+,X\right) B\left[\kappa_{\alpha\beta}(1-\nu) + \nu\delta_{\alpha\beta}\kappa_{\phi\phi}\right] w_{3,\beta}(X)d\Omega(X) \tag{2}
$$
$$
= \int_\Gamma U_{\theta\alpha}^*\left(x^+,x\right) t_\alpha(x)d\Gamma(x) + \int_\Omega U_{\theta\alpha}^*\left(x^+,X\right) q_\alpha(X)d\Omega(X)
$$

where $\fint$ represents the Cauchy principal value integral. Here, x denotes the field points. The tension stiffness is given by $B = Eh^3/[12(1-\nu)]$, where E denotes the Young's modulus, h is the thickness of the shell, and ν is the Poisson's ratio. $\kappa_{\alpha\beta}$ is the curvature. $x \in \Gamma$ and $X \in \Omega$ represent field points on the boundary and within the domain, respectively. Within the equations presented above, w_1 and w_2 denote the rotations in the x_1 and x_2 directions, respectively. w_3 corresponds to the out-of-plane displacement, while u_1 and u_2 represent in-plane displacements along the x_1 and x_2 directions. Similarly, p_1 and p_2 denote bending tractions, while p_3 denotes shear traction. Additionally, t_1 and t_2 denote membrane tractions in the x_1 and x_2 directions, respectively. The terms

q_α and q_3 refer to membrane body forces and domain pressure forces, respectively. The symbols W_{ij}^* and $U_{\theta\alpha}^*$ represent fundamental solutions for displacements, while P_{ij}^* and $T_{\theta\alpha}^{*(i)}$ represent fundamental solutions for tractions. The explicit expressions for these fundamental solutions can be found in [18].

The traction integral equations for the collocation on the lower crack surface can be written as:

$$
\frac{1}{2}p_\alpha\left(x^-\right) - \frac{1}{2}p_\alpha\left(x^+\right) + n_\beta\left(x^-\right)\fint_\Gamma P_{\alpha\beta\gamma}^*\left(x^-,x\right) w_\gamma(x)d\Gamma(x)
$$
$$
+ n_\beta\left(x^-\right)\fint_\Gamma P_{\alpha\beta3}^*\left(x^-,x\right) w_3(x)d\Gamma(x)
$$
$$
= n_\beta\left(x^-\right)\fint_\Gamma W_{\alpha\beta\gamma}^*\left(x^-,x\right) p_\gamma(x)d\Gamma(x) + n_\beta\left(x^-\right)\int_\Gamma W_{\alpha\beta3}^*\left(x^-,x\right) p_3(x)d\Gamma(x)
$$
$$
- n_\beta(x^-)\int_\Omega \kappa_{\theta\psi} B\frac{1-\nu}{2}\left(u_{\theta,\psi}(X) + u_{\psi,\theta}(X) + \frac{2\nu}{1-\nu}u_{\phi,\phi}(X)\delta_{\theta\psi}\right)
$$
$$
\times W_{\alpha\beta3}^*(x^-,X)d\Omega(X)
$$
$$
- n_\beta\left(x^-\right)\int_\Omega \kappa_{\theta\psi} B\left((1-\nu)\kappa_{\theta\psi} + \nu\delta_{\theta\psi}\kappa_{\phi\phi}\right) w_3(X)W_{\alpha\beta3}^*\left(x^-,X\right) d\Omega(X)
$$
$$
+ n_\beta\left(x^-\right)\int_\Omega W_{\alpha\beta3}^*\left(x^-,X\right) q_3 d\Omega(X) \tag{3}
$$

and

$$
\frac{1}{2}p_3\left(x^-\right) - \frac{1}{2}p_3\left(x^+\right) + n_\beta\left(x^-\right)\fint_\Gamma P_{3\beta\gamma}^*\left(x^-,x\right) w_\gamma(x)d\Gamma(x)
$$
$$
+ n_\beta\left(x^-\right)\fint_\Gamma P_{3\beta3}^*\left(x^-,x\right) w_3(x)d\Gamma(x)
$$
$$
= n_\beta\left(x^-\right)\int_\Gamma W_{3\beta\gamma}^*\left(x^-,x\right) p_\gamma(x)d\Gamma(x) + n_\beta\left(x^-\right)\fint_\Gamma W_{3\beta3}^*\left(x^-,x\right) p_3(x)d\Gamma(x)
$$
$$
- n_\beta(x^-)\int_\Omega \kappa_{\theta\psi} B\frac{1-\nu}{2}\left(u_{\theta,\psi}(X) + u_{\psi,\theta}(X) + \frac{2\nu}{1-\nu}u_{\phi,\phi}(X)\delta_{\theta\psi}\right)
$$
$$
\times W_{3\beta3}^*\left(x^-,X\right) d\Omega(X)
$$
$$
- n_\beta\left(x^-\right)\int_\Omega \kappa_{\theta\psi} B\left((1-\nu)\kappa_{\theta\psi} + \nu\delta_{\theta\psi}\kappa_{\phi\phi}\right) w_3(X)W_{3\beta3}^*\left(x^-,X\right) d\Omega(X)
$$
$$
+ n_\beta\left(x^-\right)\int_\Omega W_{3\beta3}^*\left(x^-,X\right) q_3 d\Omega(X) \tag{4}
$$

and

$$
\frac{1}{2}t_\alpha\left(x^-\right) - \frac{1}{2}t_\alpha\left(x^+\right) + n_\beta\left(x^-\right)\fint_\Gamma T_{\alpha\beta\gamma}^*\left(x^-,x\right) u_\gamma(x)d\Gamma(x)
$$
$$
+ n_\beta\left(x^-\right)\fint_\Gamma U_{\alpha\beta\gamma}^*\left(x^-,x\right) B\left[\kappa_{\theta\psi}(1-\nu) + \nu\delta_{\theta\psi}\kappa_{\phi\phi}\right] w_3(x)n_\psi(x)d\Gamma(x)
$$
$$
- n_\beta\left(x^-\right)\int_\Omega U_{\alpha\beta\gamma}^*\left(x^-,X\right) B[\kappa_{\theta\psi}(1-\nu) + \nu\delta_{\theta\psi}\kappa_{\phi\phi}]w_{3,\beta}(X)d\Omega(X) \tag{5}
$$
$$
= n_\beta\left(x^-\right)\fint_\Gamma U_{\alpha\beta\gamma}^*\left(x^-,x\right) t_\gamma(x)d\Gamma(x) + n_\beta\left(x^-\right)\int_\Omega U_{\alpha\beta\gamma}^*(x^-,X)q_\gamma d\Omega(X)
$$
$$
+ \frac{1}{2}n_\beta\left(x^-\right) B\left[(1-\nu)\kappa_{\theta\psi} + \nu\delta_{\theta\psi}\kappa_{\phi\phi}\right] w_3\left(x^-\right)
$$

The detailed expressions for the kernels $P_{\alpha\beta\gamma}^*$, $W_{\alpha\beta\gamma}^*$, $T_{\alpha\beta\gamma}^*$, and $U_{\alpha\beta\gamma}^*$ are outlined in [18]. n is the outward unit vector to the shell boundary. The symbol $\fint$ represents the Hadamard principal value. Eqs. (1) to (2) and Eqs. (3) to (5) represent the displacement and traction integral equations for collocation on the top and bottom boundaries of the crack, respectively. For the rest of the boundaries Γ^e, the collocation can be conducted using the traditional BEM formulations.

It is important to note that Eqs. (1) to (5) encompass the domain integral $\int_\Omega$. This domain integral can be transformed into a boundary integral via the application of the Dual Reciprocity Method (DRM). This process involves the utilization of the particular solutions, namely, $(\hat{u}_{m\alpha}^\gamma, \hat{t}_{m\alpha}^\gamma)$, which are derived from solving the Galerkin vector for 2D plane stress, and $(\hat{u}_{m\alpha}^i, \hat{p}_{m\alpha}^i)$ for plate bending problem, obtained through the implementation of radial basis functions.

In order to address the improper integration that appears in the boundary integral equations, specialized regularization techniques were employed. Specifically, the terms such as $W^*_{\alpha\beta3}$, $W^*_{3\beta\gamma}$, and $Q^*_{3\beta}$ exhibit a singularity of order $O(\ln(r))$, denoting a weak singularity that can be effectively managed through the Telles transformation.

Moreover, integration of the terms P^*_{ij}, $T^*_{\theta\alpha}$, $P^*_{\alpha\beta3}$, $P^*_{3\beta\gamma}$, $W^*_{\alpha\beta\gamma}$, $W^*_{3\beta3}$, $P^*_{\alpha\beta\gamma}$ arises a strong singularity of order $O(1/r)$. This strong singularity can be appropriately addressed using the singularity subtraction method, based on the first term of Taylor expansion around the singularity point. Subsequently, the singularity term can be integrated analytically, with the aid of the Cauchy principal value.

Furthermore, the integration of $T^{(i)*}_{\alpha\beta\gamma}$ introduces a hypersingular term of order $O(1/r^2)$. The singularity subtraction method remains applicable in this case, incorporating both the first and second terms of the Taylor expansion around the singularity. Allowing for analytical integration via the Hadamard principal value.

Lastly, for the remaining terms, namely, $P^*_{\alpha\beta\gamma}$ and $P^*_{3\beta3}$, which exhibit a singularity of order $O(1/r^2 + \ln(r))$, the separation approach is applied, effectively separating the hypersingular and weakly singular components and the corresponding regularization approach can be applied.

The basic DBEM of the shallow shell was proposed by Dirgantara [18] and further improved by Wen [21]. The details and comprehensive insights into the DRM formulation and the treatment of singularity are provided in the corresponding reference.

The formulations applied in the DBEM employ a system of equations denoted as $\mathbf{Hu} = \mathbf{Gt}$, in which $\mathbf{H}$ and $\mathbf{G}$ represent the coefficient matrices. The vectors $\mathbf{u}$ and $\mathbf{t}$ encompass both known and unknown displacements and tractions. By rearranging the system equation, a vector labelled as $\mathbf{X}$ is introduced to encompass all the unknowns, while vector $\mathbf{F}$ contains all the known boundary displacements and tractions. As a result, the system of equations can be succinctly reformulated as:

$$\mathbf{AX} = \mathbf{F} \tag{6}$$

2.2. DBEM-based IDM formulations with respect to geometric variable Z_g for shallow shells

A critical aspect of the FORM is to evaluate the sensitivity of the limit state function to various design parameters. This section presents the derivatives of the DBEM boundary integral equations with respect to geometrical variables.

Changing the geometrical parameters does not affect the values of the curvature, therefore for simplification, the constant term $C_{\kappa1} = B\left((1-\nu)\kappa_{\alpha\beta} + \nu\delta_{\alpha\beta}\kappa_{\phi\phi}\right)$ is introduced. The derivatives of the DBEM displacement integral equations applied for collocations on the upper crack surfaces (as given in Eqs. (1) to (2)) are:

$$
\frac{1}{2}w_{j,g}\left(x^+\right) + \frac{1}{2}w_{j,g}\left(x^-\right) + \fint_{\Gamma}\left[P^*_{ij,g}w_j + P^*_{ij}w_{j,g}\right]d\Gamma
$$
$$
= \int_{\Gamma}\left[W^*_{ij,g}p_j + W^*_{ij}p_{j,g}\right]d\Gamma
$$
$$
- \int_{\Omega}W^*_{i3,g}\kappa_{\alpha\beta}B\frac{1-\nu}{2}\left[u_{\alpha,\beta} + u_{\beta,\alpha} + \frac{2\nu}{1-\nu}u_{\phi,\phi}\delta_{\alpha\beta}\right]d\Omega
$$
$$
- \int_{\Omega}W^*_{i3}\kappa_{\alpha\beta}B\frac{1-\nu}{2}\left[u_{\alpha,\beta g} + u_{\beta,\alpha g} + \frac{2\nu}{1-\nu}u_{\phi,\phi g}\delta_{\alpha\beta}\right]d\Omega
$$
$$
- \int_{\Omega}\left[W^*_{i3,g}\kappa_{\alpha\beta}C_{\kappa1}w_3 + W^*_{i3}\kappa_{\alpha\beta}C_{\kappa1}w_{3,g}\right]d\Omega
$$
$$
+ \int_{\Omega}\left[W^*_{i3,g}q_3 + W^*_{i3}q_{3,g}\right]d\Omega \tag{7}
$$

and

$$
\frac{1}{2}u_{\alpha,g}\left(x^+\right) + \frac{1}{2}u_{\alpha,g}\left(x^-\right) + \fint_{\Gamma}\left[T^*_{\theta\alpha,g}u_\alpha + T^*_{\theta\alpha}u_{\alpha,g}\right]d\Gamma
$$
$$
+ \int_{\Gamma}\left[U^*_{\theta\alpha,g}C_{\kappa1}w_3n_\beta + U^*_{\theta\alpha}C_{\kappa1}w_{3,g}n_\beta + U^*_{\theta\alpha}C_{\kappa1}w_3n_{\beta,g}\right]d\Gamma
$$
$$
- \int_{\Omega}\left[U^*_{\theta\alpha,g}C_{\kappa1}w_{3,\beta} + U^*_{\theta\alpha}C_{\kappa1}w_{3,\beta g}\right]d\Omega \tag{8}
$$
$$
= \int_{\Gamma}\left[U^*_{\theta\alpha,g}t_\alpha + U^*_{\theta\alpha}t_{\alpha,g}\right]d\Gamma + \int_{\Omega}\left[U^*_{\theta\alpha,g}q_\alpha + U^*_{\theta\alpha}q_{\alpha,g}\right]d\Omega
$$

Similarly, the constant term $C_{\kappa2} = B\left((1-\nu)\kappa_{\theta\psi} + \nu\delta_{\theta\psi}\kappa_{\phi\phi}\right)$ is introduced. The derivatives of the DBEM traction integral equations for collocations on the lower crack surfaces (Eqs. (3) to (5)) are:

$$
\frac{1}{2}p_{\alpha,g}\left(x^-\right) - \frac{1}{2}p_{\alpha,g}\left(x^+\right) + n_{\beta,g}\left(x^-\right)\fint_{\Gamma}P^*_{\alpha\beta\gamma}w_\gamma d\Gamma
$$
$$
+ n_\beta\left(x^-\right)\fint_{\Gamma}\left[P^*_{\alpha\beta\gamma,g}w_\gamma + P^*_{\alpha\beta\gamma}w_{\gamma,g}\right]d\Gamma
$$
$$
+ n_{\beta,g}\left(x^-\right)\fint_{\Gamma}P^*_{\alpha\beta3}w_3 d\Gamma + n_\beta\left(x^-\right)\int_{\Gamma}\left[P^*_{\alpha\beta3,g}w_3 + P^*_{\alpha\beta3}w_{3,g}\right]d\Gamma
$$
$$
= n_{\beta,g}\left(x^-\right)\fint_{\Gamma}W^*_{\alpha\beta\gamma}p_\gamma d\Gamma + n_\beta\left(x^-\right)\fint_{\Gamma}\left[W^*_{\alpha\beta\gamma,g}p_\gamma + W^*_{\alpha\beta\gamma}p_{\gamma,g}\right]d\Gamma
$$
$$
+ n_{\beta,g}\left(x^-\right)\int_{\Gamma}W^*_{\alpha\beta3}p_3 d\Gamma + n_\beta\left(x^-\right)\int_{\Gamma}\left[W^*_{\alpha\beta3,g}p_3 + W^*_{\alpha\beta3}p_{3,g}\right]d\Gamma
$$
$$
- n_{\beta,g}\left(x^-\right)\int_{\Omega}\kappa_{\theta\psi}B\frac{1-\nu}{2}\left(u_{\theta,\psi} + u_{\psi,\theta} + \frac{2\nu}{1-\nu}u_{\phi,\phi}\delta_{\theta\psi}\right)W^*_{\alpha\beta3}d\Omega \tag{9}
$$
$$
- n_\beta\left(x^-\right)\int_{\Omega}\kappa_{\theta\psi}B\frac{1-\nu}{2}\left(u_{\theta,\psi g} + u_{\psi,\theta g} + \frac{2\nu}{1-\nu}u_{\phi,\phi g}\delta_{\theta\psi}\right)W^*_{\alpha\beta3}d\Omega
$$
$$
- n_\beta\left(x^-\right)\int_{\Omega}\kappa_{\theta\psi}B\frac{1-\nu}{2}\left(u_{\theta,\psi} + u_{\psi,\theta} + \frac{2\nu}{1-\nu}u_{\phi,\phi}\delta_{\theta\psi}\right)W^*_{\alpha\beta3,g}d\Omega
$$
$$
- n_{\beta,g}\left(x^-\right)\int_{\Omega}\kappa_{\theta\psi}C_{\kappa2}w_3 W^*_{\alpha\beta3}d\Omega
$$
$$
- n_\beta\left(x^-\right)\int_{\Omega}\kappa_{\theta\psi}C_{\kappa2}\left[w_{3,g}W^*_{\alpha\beta3} + w_3 W^*_{\alpha\beta3,g}\right]d\Omega
$$
$$
+ n_{\beta,g}\left(x^-\right)\int_{\Omega}W^*_{\alpha\beta3}q_3 d\Omega + n_\beta\left(x^-\right)\int_{\Omega}\left[W^*_{\alpha\beta3,g}q_3 + W^*_{\alpha\beta3}q_{3,g}\right]d\Omega
$$

and

$$
\frac{1}{2}p_{3,g}\left(x^-\right) - \frac{1}{2}p_{3,g}\left(x^+\right) + n_{\beta,g}\left(x^-\right)\fint_{\Gamma}P^*_{3\beta\gamma}w_\gamma d\Gamma
$$
$$
+ n_\beta\left(x^-\right)\fint_{\Gamma}\left[P^*_{3\beta\gamma,g}w_\gamma + P^*_{3\beta\gamma}w_{\gamma,g}\right]d\Gamma
$$
$$
+ n_{\beta,g}\left(x^-\right)\fint_{\Gamma}P^*_{3\beta3}w_3 d\Gamma + n_\beta\left(x^-\right)\fint_{\Gamma}\left[P^*_{3\beta3,g}w_3 + P^*_{3\beta3}w_{3,g}\right]d\Gamma
$$
$$
= n_{\beta,g}\left(x^-\right)\int_{\Gamma}W^*_{3\beta\gamma}p_\gamma d\Gamma + n_\beta\left(x^-\right)\int_{\Gamma}\left[W^*_{3\beta\gamma,g}p_\gamma + W^*_{3\beta3}p_{\gamma,g}\right]d\Gamma
$$
$$
+ n_{\beta,g}\left(x^-\right)\fint_{\Gamma}W^*_{3\beta3}p_3 d\Gamma + n_\beta\left(x^-\right)\fint_{\Gamma}\left[W^*_{3\beta3,g}p_3 + W^*_{3\beta3}p_{3,g}\right]d\Gamma
$$
$$
- n_{\beta,g}\left(x^-\right)\int_{\Omega}\kappa_{\theta\psi}B\frac{1-\nu}{2}\left(u_{\theta,\psi} + u_{\psi,\theta} + \frac{2\nu}{1-\nu}u_{\phi,\phi}\delta_{\theta\psi}\right)W^*_{3\beta3}d\Omega \tag{10}
$$
$$
- n_\beta\left(x^-\right)\int_{\Omega}\kappa_{\theta\psi}B\frac{1-\nu}{2}\left[\left(u_{\theta,\psi g} + u_{\psi,\theta g} + \frac{2\nu}{1-\nu}u_{\phi,\phi g}\delta_{\theta\psi}\right)W^*_{3\beta3}\right.
$$
$$
\left. + \left(u_{\theta,\psi} + u_{\psi,\theta} + \frac{2\nu}{1-\nu}u_{\phi,\phi}\delta_{\theta\psi}\right)W^*_{3\beta3,g}\right]d\Omega
$$
$$
- n_{\beta,g}\left(x^-\right)\int_{\Omega}\kappa_{\theta\psi}C_{\kappa2}w_3 W^*_{3\beta3}d\Omega
$$
$$
- n_\beta\left(x^-\right)\int_{\Omega}\kappa_{\theta\psi}C_{\kappa2}\left[w_{3,g}W^*_{3\beta3} + w_3 W^*_{3\beta3,g}\right]d\Omega
$$
$$
+ n_{\beta,g}\left(x^-\right)\int_{\Omega}W^*_{3\beta3}q_3 d\Omega + n_\beta\left(x^-\right)\int_{\Omega}\left[W^*_{3\beta3,g}q_3 + W^*_{3\beta3}q_{3,g}\right]d\Omega
$$

and

$$\frac{1}{2}t_{\alpha,g}\left(x^-\right) - \frac{1}{2}t_{\alpha,g}\left(x^+\right) + n_{\beta,g}\left(x^-\right)\fint_\Gamma T^*_{\alpha\beta\gamma}u_\gamma d\Gamma$$

$$+ n_\beta\left(x^-\right)\fint_\Gamma \left[T^*_{\alpha\beta\gamma,g}u_\gamma + T^*_{\alpha\beta\gamma}u_{\gamma,g}\right]d\Gamma$$

$$+ n_{\beta,g}\left(x^-\right)\fint_\Gamma U^*_{\alpha\beta\gamma}C_{\kappa2}w_3 n_\psi(x)d\Gamma + n_\beta\left(x^-\right)\fint_\Gamma U^*_{\alpha\beta\gamma,g}C_{\kappa2}w_3 n_\psi d\Gamma$$

$$+ n_\beta\left(x^-\right)\fint_\Gamma U^*_{\alpha\beta\gamma}C_{\kappa2}\left[w_{3,g}n_\psi(x) + w_3 n_{\psi,g}\right]d\Gamma$$

$$- n_{\beta,g}\left(x^-\right)\int_\Omega U^*_{\alpha\beta\gamma}C_{\kappa2}w_{3,\beta}d\Omega \qquad (11)$$

$$- n_\beta\left(x^-\right)\int_\Omega \left[U^*_{\alpha\beta\gamma,g}C_{\kappa2}w_{3,\beta} + U^*_{\alpha\beta\gamma}C_{\kappa2}w_{3,\beta g}\right]d\Omega$$

$$= n_{\beta,g}\left(x^-\right)\fint_\Gamma U^*_{\alpha\beta\gamma}t_\gamma d\Gamma + n_\beta\left(x^-\right)\fint_\Gamma \left[U^*_{\alpha\beta\gamma,g}t_\gamma + U^*_{\alpha\beta\gamma}t_{\gamma,g}\right]d\Gamma$$

$$+ n_{\beta,g}\left(x^-\right)\int_\Omega U^*_{\alpha\beta\gamma}q_\gamma d\Omega + n_\beta\left(x^-\right)\int_\Omega \left[U^*_{\alpha\beta\gamma,g}q_\gamma + U^*_{\alpha\beta\gamma}q_{\gamma,g}\right]d\Omega$$

$$+ \frac{1}{2}n_{\beta,g}\left(x^-\right)C_{\kappa2}w_3\left(x^-\right) + \frac{1}{2}n_\beta\left(x^-\right)C_{\kappa2}w_{3,g}\left(x^-\right)$$

The notation $()_{,g}$ represents the derivatives with respect to Z_g. The expressions for the derivatives of the fundamental solutions and kernels can be found in the work by Morse [35], which addresses plate bending problems. Additionally, the derivatives of the particular solutions for the DRM can be found in previous work [39].

The system of equations for the IDM-based DBEM formulation is represented as $\mathbf{H}_{,g}\mathbf{u} + \mathbf{H}\mathbf{u}_{,g} = \mathbf{G}_{,g}\mathbf{t} + \mathbf{G}\mathbf{t}_{,g}$. Here, the definitions of the terms $\mathbf{H}$, $\mathbf{G}$, $\mathbf{t}$, and $\mathbf{u}$ remain consistent with those presented in Section 2.1. The terms $\mathbf{H}_{,g}$, $\mathbf{G}_{,g}$, $\mathbf{t}_{,g}$, and $\mathbf{u}_{,g}$ correspond to the derivatives of the above-mentioned terms. This system of equations can be rearranged as:

$$\mathbf{AX}_{,g} = \mathbf{F}_{,g} - \mathbf{A}_{,g}\mathbf{X} \qquad (12)$$

where the system matrices $\mathbf{A}$ and $\mathbf{X}$ can be obtained from Eq. (6). The displacement and traction integral equations are formulated with respect to the nodal coordinates of both the collocation and field points. The derivatives of these integral equations are influenced by the changes in these nodal coordinates. Thus, if a change in the geometrical variable Z_g does not change the nodal coordinates of both the collocation point and the field point on a given boundary (such as curvature and thickness), the associated elements within $\mathbf{X}_{,g}$ will become null. As a result, calculations for entries corresponding to such nodal points do not need to be conducted, leading to a reduction in computational expenses.

2.3. DBEM-based IDM formulations with respect to curvature Z_ρ for shallow shells

The derivatives of the DBEM formulation with respect to changes in curvature, denoted as Z_ρ, were derived in a similar approach as for changes in the geometrical variable Z_g. The curvatures considered in this study are limited to the x and y directions, such that $\kappa_{11} \neq 0$ and $\kappa_{22} \neq 0$, while $\kappa_{12} = \kappa_{21} = 0$. As a result, the variable ρ can only take values of κ_{11} and κ_{22}. The derivatives of curvature can be simplified as $\kappa_{\alpha\beta,\rho} = \delta_{\alpha\rho}\delta_{\beta\rho}$. A similar approach was applied to derive the derivatives of the boundary integral equation as presented in the previous section. It is worth noting that the fundamental solutions, kernels and the DRM formulations are not affected by changes in the value of the curvature.

The derivatives of the DBEM displacement integral equation for collocations on the upper crack surface with respect to curvature are as follows:

$$\frac{1}{2}w_{j,\rho}\left(x^+\right) + \frac{1}{2}w_{j,\rho}\left(x^-\right) + \fint_\Gamma P^*_{ij}w_{j,\rho}d\Gamma$$

$$= \int_\Gamma W^*_{ij}p_{j,\rho}d\Gamma$$

$$- \int_\Omega W^*_{i3}\kappa_{\alpha\beta,\rho}B\frac{1-\nu}{2}\left[u_{\alpha,\beta} + u_{\beta,\alpha} + \frac{2\nu}{1-\nu}u_{\phi,\phi}\delta_{\alpha\beta}\right]d\Omega$$

$$- \int_\Omega W^*_{i3}\kappa_{\alpha\beta}B\frac{1-\nu}{2}\left[u_{\alpha,\beta\rho} + u_{\beta,\alpha\rho} + \frac{2\nu}{1-\nu}u_{\phi,\phi\rho}\delta_{\alpha\beta}\right]d\Omega \qquad (13)$$

$$- \int_\Omega W^*_{i3}\left[\kappa_{\alpha\beta,\rho}C_{\kappa1}w_3 + \kappa_{\alpha\beta}C_{\kappa1,\rho}w_3 + \kappa_{\alpha\beta}C_{\kappa1}w_{3,\rho}\right]d\Omega$$

$$+ \int_\Omega W^*_{i3}q_{3,\rho}d\Omega$$

and

$$\frac{1}{2}u_{\alpha,\rho}\left(x^+\right) + \frac{1}{2}u_{\alpha,\rho}\left(x^-\right) + \fint_\Gamma T^*_{\theta\alpha}u_{\alpha,\rho}d\Gamma$$

$$+ \int_\Gamma U^*_{\theta\alpha}\left[C_{\kappa1,\rho}w_3 + C_{\kappa1}w_{3,\rho}\right]n_\beta d\Gamma$$

$$- \int_\Omega U^*_{\theta\alpha}\left[C_{\kappa1,\rho}w_{3,\beta} + C_{\kappa1}w_{3,\rho\beta}\right]d\Omega \qquad (14)$$

$$= \int_\Gamma U^*_{\theta\alpha}t_{\alpha,\rho}d\Gamma + \int_\Omega U^*_{\theta\alpha}q_{\alpha,\rho}d\Omega$$

where $C_{\kappa1,\rho} = B\left[\kappa_{\alpha\beta,\rho}(1-\nu) + \nu\delta_{\alpha\beta}\kappa_{\phi\phi,\rho}\right]$. The notation $()_{,\rho}$ represents the derivatives with respect to curvature Z_ρ.

The derivatives of the DBEM traction integral equation for collocations on the lower crack surface with respect to the curvature is:

$$\frac{1}{2}p_{\alpha,\rho}\left(x^-\right) - \frac{1}{2}p_{\alpha,\rho}\left(x^+\right) + n_\beta\left(x^-\right)\fint_\Gamma P^*_{\alpha\beta\gamma}w_{\gamma,\rho}d\Gamma$$

$$+ n_\beta\left(x^-\right)\fint_\Gamma P^*_{\alpha\beta3}w_{3,\rho}d\Gamma$$

$$= n_\beta\left(x^-\right)\fint_\Gamma W^*_{\alpha\beta\gamma}p_{\gamma,\rho}d\Gamma + n_\beta\left(x^-\right)\int_\Gamma W^*_{\alpha\beta3}p_{3,\rho}d\Gamma$$

$$- n_\beta(x^-)\int_\Omega \kappa_{\theta\psi,\rho}B\frac{1-\nu}{2}\left(u_{\theta,\psi} + u_{\psi,\theta} + \frac{2\nu}{1-\nu}u_{\phi,\phi}\delta_{\theta\psi}\right)W^*_{\alpha\beta3}d\Omega \qquad (15)$$

$$- n_\beta(x^-)\int_\Omega \kappa_{\theta\psi}B\frac{1-\nu}{2}\left(u_{\theta,\psi\rho} + u_{\psi,\theta\rho} + \frac{2\nu}{1-\nu}u_{\phi,\phi\rho}\delta_{\theta\psi}\right)W^*_{\alpha\beta3}d\Omega$$

$$- n_\beta\left(x^-\right)\int_\Omega \left[\kappa_{\theta\psi,\rho}C_{\kappa2}w_3 + \kappa_{\theta\psi}C_{\kappa2,\rho}w_3 + \kappa_{\theta\psi}C_{\kappa2}w_{3,\rho}\right]W^*_{\alpha\beta3}d\Omega$$

$$+ n_\beta\left(x^-\right)\int_\Omega W^*_{\alpha\beta3}q_{3,\rho}d\Omega$$

and

$$\frac{1}{2}p_{3,\rho}\left(x^-\right) - \frac{1}{2}p_{3,\rho}\left(x^+\right) + n_\beta\left(x^-\right)\fint_\Gamma P^*_{3\beta\gamma}w_{\gamma,\rho}d\Gamma$$

$$+ n_\beta\left(x^-\right)\fint_\Gamma P^*_{3\beta3}w_{3,\rho}d\Gamma$$

$$= n_\beta\left(x^-\right)\int_\Gamma W^*_{3\beta\gamma}p_{\gamma,\rho}d\Gamma + n_\beta\left(x^-\right)\fint_\Gamma W^*_{3\beta3}p_{3,\rho}d\Gamma$$

$$- n_\beta(x^-)\int_\Omega \kappa_{\theta\psi,\rho}B\frac{1-\nu}{2}\left(u_{\theta,\psi} + u_{\psi,\theta} + \frac{2\nu}{1-\nu}u_{\phi,\phi}\delta_{\theta\psi}\right)W^*_{3\beta3}d\Omega$$

$$- n_\beta(x^-)\int_\Omega \kappa_{\theta\psi}B\frac{1-\nu}{2}\left(u_{\theta,\psi\rho} + u_{\psi,\theta\rho} + \frac{2\nu}{1-\nu}u_{\phi,\phi\rho}(X)\delta_{\theta\psi}\right)W^*_{3\beta3}d\Omega$$

$$- n_\beta\left(x^-\right)\int_\Omega \left[\kappa_{\theta\psi,\rho}C_{\kappa2}w_3 + \kappa_{\theta\psi}C_{\kappa2,\rho}w_3 + \kappa_{\theta\psi}C_{\kappa2}w_{3,\rho}\right]W^*_{3\beta3}d\Omega$$

$$+ n_\beta\left(x^-\right)\int_\Omega W^*_{3\beta3}q_{3,\rho}d\Omega$$

$$(16)$$

and

$$\frac{1}{2}t_{\alpha,\rho}(x^-) - \frac{1}{2}t_{\alpha,\rho}(x^+) + n_\beta(x^-)\fint_\Gamma T^*_{\alpha\beta\gamma}u_{\gamma,\rho}d\Gamma$$

$$+ n_\beta(x^-)\fint_\Gamma U^*_{\alpha\beta\gamma}\left[C_{\kappa2,\rho}w_3 + C_{\kappa2}w_{3,\rho}\right]n_\psi d\Gamma$$

$$- n_\beta(x^-)\int_\Omega U^*_{\alpha\beta\gamma}\left[C_{\kappa2,\rho}w_{3,\beta} + C_{\kappa2}w_{3,\beta\rho}\right]d\Omega \qquad (17)$$

$$= n_\beta(x^-)\fint_\Gamma U^*_{\alpha\beta\gamma}t_{\gamma,\rho}d\Gamma + n_\beta(x^-)\int_\Omega U^*_{\alpha\beta\gamma}q_{\gamma,\rho}d\Omega$$

$$+ \frac{1}{2}n_\beta(x^-)\left[C_{\kappa2,\rho}w_3(x^-) + C_{\kappa2}w_{3,\rho}(x^-)\right]$$

where $C_{\kappa2,\rho} = B\left((1-\nu)\kappa_{\theta\psi,\rho} + \nu\delta_{\theta\psi,\rho}\kappa_{\phi\phi,\rho}\right)$. In terms of the formation of the system matrix, the sensitivity of the SIFs is the same as for the derivative with respect to a geometrical variable.

2.4. Stress intensity factor sensitivities

The Crack Surface Displacement Extrapolation technique (CSDE) method, as being applied in [40], has been assessed for its accuracy in comparison to both experimental data and results derived from the J-integral method. This evaluation focused on a plate under multi-axial loading conditions. The findings revealed that the CSDE technique is capable of achieving a level of accuracy comparable to that of the J-integral method, with the observed error being less than 1%. Furthermore, it was noted that the accuracy of the CSDE method improved with the use of a finer mesh in the structure, indicating its efficiency and effectiveness in structural analysis. The CSDE has been employed in this study to assess the stress intensity factor at the crack tip.

The stress intensity factor K can be expressed in relation to the displacements present on the crack surfaces adjacent to the crack tip, as follows:

$$\{K\} = \frac{1}{\sqrt{r}}[C]\{\Delta w\} \qquad (18)$$

$$\{K\} = \begin{Bmatrix} K_{1b} \\ K_{2b} \\ K_{3b} \\ K_{1m} \\ K_{2m} \end{Bmatrix}, \quad \{\Delta w\} = \begin{Bmatrix} \Delta\phi_2 \\ \Delta\phi_1 \\ \Delta w_3 \\ \Delta u_2 \\ \Delta u_1 \end{Bmatrix} \qquad (19)$$

where

$$\begin{Bmatrix} \Delta\phi_2 \\ \Delta\phi_1 \\ \Delta w_3 \\ \Delta u_2 \\ \Delta u_1 \end{Bmatrix} = \begin{Bmatrix} \phi_2 \\ \phi_1 \\ w_3 \\ u_2 \\ u_1 \end{Bmatrix}_{\theta=180°} - \begin{Bmatrix} \phi_2 \\ \phi_1 \\ w_3 \\ u_2 \\ u_1 \end{Bmatrix}_{\theta=-180°} \qquad (20)$$

ϕ_1 and ϕ_2 are the rotations in x and y directions respectively. w_3 is the out-of-plane displacement. u_1 and u_2 are the in-plane displacements in the x and y direction respectively.

$$[\mathbf{C}] = \begin{bmatrix} \frac{Eh^3}{48}\sqrt{\frac{\pi}{2}} & 0 & 0 & 0 & 0 \\ 0 & \frac{Eh^3}{48}\sqrt{\frac{\pi}{2}} & 0 & 0 & 0 \\ 0 & 0 & \frac{5Eh}{24(1+\nu)}\sqrt{\frac{\pi}{2}} & 0 & 0 \\ 0 & 0 & 0 & \frac{Eh}{8}\sqrt{2\pi} & 0 \\ 0 & 0 & 0 & 0 & \frac{Eh}{8}\sqrt{2\pi} \end{bmatrix} \qquad (21)$$

An illustration of the crack tip element is presented in Fig. 2. The crack tip stress intensity factors can be extrapolated from $\{K\}^{AA'}$ and $\{K\}^{BB'}$ by substituting the boundary displacements and rotation using Eq. (18), where:

$$\{K\}^{AA'} = \sqrt{\frac{6}{5l}}[\mathbf{C}]\left(\{w\}^A - \{w\}^{A'}\right)$$
$$\{K\}^{BB'} = \sqrt{\frac{2}{l}}[\mathbf{C}]\left(\{w\}^B - \{w\}^{B'}\right) \qquad (22)$$
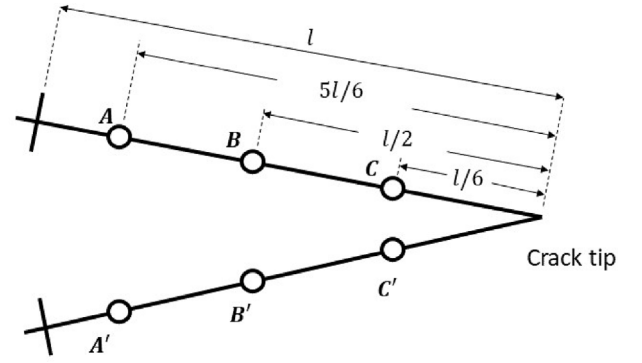

Fig. 2. Example of crack tip nodal element.

where l is the crack tip element length. The value of the stress intensity factor at the crack tip can be extrapolated as:

$$\{K\}^{tip} = \frac{r_{AA'}}{r_{AA'} - r_{BB'}}\left(\{K\}^{BB'} - \frac{r_{BB'}}{r_{AA'}}\{K\}^{AA'}\right) \qquad (23)$$

where $r_{AA'} = 5l/6$ and $r_{BB'} = l/2$. It is worth noting that the selection of points AA' BB' does not necessarily need to take the same values as provided above. and The stress intensity factors at the crack tip can be extrapolated from any point within the crack tip element by substituting the corresponding distance from the crack tip.

The sensitivity of the stress intensity factors with respect to certain geometrical variables or curvature can be derived from the above equation. The derivatives of $\{K\}$ can be expressed as:

$$K_{1b,g} = \frac{Eh^3}{48\sqrt{r}}\sqrt{\frac{\pi}{2}}\left\{\Delta\phi_{2,g} - \frac{r_{,g}}{2r}\Delta\phi_2\right\}$$

$$K_{2b,g} = \frac{Eh^3}{48\sqrt{r}}\sqrt{\frac{\pi}{2}}\left\{\Delta\phi_{1,g} - \frac{r_{,g}}{2r}\Delta\phi_1\right\}$$

$$K_{3b,g} = \frac{5Eh}{24(1+\nu)\sqrt{r}}\sqrt{\frac{\pi}{2}}\left\{\Delta w_{3,g} - \frac{r_{,g}}{2r}\Delta w_3\right\} \qquad (24)$$

$$K_{1m,g} = \frac{Eh\sqrt{2\pi}}{8\sqrt{r}}\left\{\Delta u_{2,g} - \frac{r_{,g}}{2r}\Delta u_2\right\}$$

$$K_{2m,g} = \frac{Eh\sqrt{2\pi}}{8\sqrt{r}}\left\{\Delta u_{1,g} - \frac{r_{,g}}{2r}\Delta u_1\right\}$$

By applying the extrapolation in Eq. (23), the sensitivities of the stress intensity factors are:

$$\{K\}^{tip}_{,g} = RRB_{,g}\{K\}^{BB'} + RRB\{K\}^{BB'}_{,g} - RRA_{,g}\{K\}^{AA'} - RRA\{K\}^{AA'}_{,g} \qquad (25)$$

where

$$RRA = \frac{r_{BB'}}{r_{AA'} - r_{BB'}} \qquad RRB = \frac{r_{AA'}}{r_{AA'} - r_{BB'}}$$

$$RRA_{,g} = \frac{r_{BB',g}}{r_{AA'} - r_{BB'}} - \frac{r_{BB'}(r_{AA',g} - r_{BB',g})}{(r_{AA'} - r_{BB'})^2} \qquad (26)$$

$$RRB_{,g} = \frac{r_{AA',g}}{r_{AA'} - r_{BB'}} - \frac{r_{AA'}(r_{AA',g} - r_{BB',g})}{(r_{AA'} - r_{BB'})^2}$$

The sensitivities of the maximum stress intensity factors were taken into consideration. The maximum SIFs were found at both the upper and lower surfaces of the shell. For this study, the SIF at the upper surface was considered, and the maximum SIF across the thickness of the shell is given by:

$$[1 + \frac{h}{4}(\frac{1}{R_1} + \frac{1}{R_2})]K_I^{max} = \frac{1}{h}K_{1m} + \frac{6}{h^2}K_{1b}$$

$$[1 + \frac{h}{4}(\frac{1}{R_1} + \frac{1}{R_2})]K_{II}^{max} = \frac{1}{h}K_{2m} + \frac{6}{h^2}K_{2b} \qquad (27)$$

$$[1 + \frac{h}{4}(\frac{1}{R_1} + \frac{1}{R_2})]K_{III}^{max} = \frac{3}{2h}K_{3b}$$

Note that the curvature-related term is introduced there $T_R = [1 + \frac{h}{4}(\frac{1}{R_1} + \frac{1}{R_2})]^{-1}$. The maximum SIF of K for different fracture modes can be found by dividing the term T_R. The derivatives of the maximum SIF can be found by:

$$K_{I,g}^{max} = \frac{T_R}{h} K_{1m,g} + \frac{6T_R}{h^2} K_{1b,g}$$

$$K_{II,g}^{max} = \frac{T_R}{h} K_{2m,g} + \frac{6T_R}{h^2} K_{2b,g} \tag{28}$$

$$K_{III,g}^{max} = \frac{3T_R}{2h} K_{3b,g}$$

Similarly, $K_{,g}^{max}$ for different fracture modes can be found by separating the terms for each mode of SIF on the right-hand side of Eq. (28). The corresponding individual maximum SIF for different fracture modes are denoted as K_{Im}, K_{IIm}, K_{Ib}, K_{IIb}, and K_{IIIb}. The derivatives of the maximum SIF with respect to curvature and thickness are given in Appendix. The effective SIF can be calculated by considering the contribution from both the bending and tension stresses.

$$K_{eff} = \sqrt{EG_{eff}} \tag{29}$$

where G_{eff} is the effective energy release rate:

$$G_{eff} = G_1 + \alpha(G_2 + G_3 + G_4 + G_5) \tag{30}$$

$$\alpha = \sqrt{\frac{|\Delta K_{Ib}|}{|\Delta K_{Ib}| + |\Delta K_{Im}|}} \tag{31}$$

The energy release rate components were defined as:

$$G_1 = \frac{K_{Im}^2}{E}, \quad G_2 = \frac{K_{IIm}^2}{E}, \quad G_3 = \frac{\pi K_{Ib}^2}{3E},$$

$$G_4 = \frac{\pi K_{IIb}^2}{E}, \quad G_5 = \frac{8\pi(1+\nu)K_{IIIb}^2}{5E} \tag{32}$$

The derivatives of the effective SIF with respect to the change in some geometrical variable can be calculated as:

$$K_{eff,g} = \frac{E}{2K_{eff}} G_{eff,g} \tag{33}$$

The derivatives of the energy release rate components are:

$$G_{1,g} = \frac{2}{E} K_{Im} K_{Im,g}$$

$$G_{2,g} = \frac{2}{E} K_{IIm} K_{IIm,g}$$

$$G_{3,g} = \frac{2\pi}{3E} K_{Ib} K_{Ib,g} \tag{34}$$

$$G_{4,g} = \frac{2\pi}{E} K_{IIb} K_{IIb,g}$$

$$G_{5,g} = \frac{16(1+\nu)\pi}{5E} K_{IIIb} K_{IIIb,g}$$

where

$$\alpha_{,g} = \frac{1}{2\alpha} \frac{|\Delta K_{Ib,g}|(|\Delta K_{Ib}| + |\Delta K_{Im}|) - |\Delta K_{Ib}|(|\Delta K_{Ib,g}| + |\Delta K_{Im,g}|)}{(|\Delta K_{Ib}| + |\Delta K_{Im}|)^2} \tag{35}$$

The derivatives of the stress intensity factors with respect to the curvature and thickness were derived using the same method.

2.5. DBEM-based FDM formulations for shallow shells

The estimation of the first-order derivatives of the SIFs, denoted as K, concerning changes in non-geometrical and non-curvature variables, was performed using the first-order finite difference method. The derivatives for FDM can be expressed as:

$$\frac{\partial K(Z_g)}{\partial Z_g} = K_{,g} = \frac{K(Z_g + \Delta Z_g) - K(Z_g - \Delta Z_g)}{2\Delta Z_g} \tag{36}$$

where ΔZ_g represents the step size. The selection of this step size has a significant impact on the accuracy of the derivatives. The step size was

adaptively chosen based on the magnitude of the variable Z_g, resulting in $\Delta Z_g = Z_g \Delta Z_g'$, where $\Delta Z_g'$ denotes the normalized step size. To identify the most suitable normalized step size, a series of convergence tests were conducted prior to the application into the FORM.

2.6. First-Order Reliability Analysis (FORM)

The primary objective of the FORM is to assess the reliability index, a parameter which represents the ability of a structure to maintain its safety throughout the operational lifespan. This index is directly associated with the probability of failure, providing a quantification of the potential risk of structural collapse.

Within the field of reliability analysis, the probabilistic space defined by the random variables $\mathbf{Z}$ can be partitioned into two regions: a failure region where $g(\mathbf{Z}) \leq 0$, and a safe region where $g(\mathbf{Z}) > 0$. The function $g(\mathbf{Z}) = 0$ serves as the performance boundary that separates these two regions. The performance function is typically formulated in terms of the structural resistance $R(\mathbf{Z})$ and the structural demand $G(\mathbf{Z})$. Common examples of structural resistance involve yield strength, maximum allowable stress, or deflection. Mathematically, the performance function or limit state function (LSF) can be expressed as:

$$g(\mathbf{Z}) = R(\mathbf{Z}) - G(\mathbf{Z}) \tag{37}$$

The probability of failure is defined as the probability that the performance function $g(\mathbf{Z}) \leq 0$ such that:

$$P_F = P\{g(\mathbf{Z}) \leq 0\} = \int_{g(\mathbf{Z})\leq 0} f_Z(\mathbf{Z})dZ \tag{38}$$

Here, $f_Z(\mathbf{Z})$ is the joint probability density function formed by all parameters in $\mathbf{Z}$. P_F represents the failure probability and its complement P_R represents the reliability, given by $1 - P_F$. The expression involves an integration over the domain where $g(\mathbf{Z}) > 0$. The evaluation of this integral can be challenging, especially considering that the design variable vector could be multidimensional. To mitigate this challenge, the FORM employs a transformation of the random variables into a standardized coordinate system known as the U-space, using the Rosenblatt transformation [41]. This transformation assumes that the Cumulative Distribution Functions (CDFs) of the random variables remain unchanged. For example, in the scenario where a variable follows a normal distribution, $Z_i \sim N(\mu_i, \sigma_i)$, the U-space is connected to the Z-space through the equation $Z_i = \mu_i + \sigma_i U_i$. In the case of a lognormal distribution, the transformation is given by $Z_i = exp(\mu_i + \sigma_i U_i)$. Consequently, Eq. (38) is transformed into the U-space as:

$$P_F = P\{g(\mathbf{U}) \leq 0\} = \int_{g(\mathbf{U})\leq 0} f_U(\mathbf{U})dU \tag{39}$$

The performance function can be approximated by the first-order Taylor expansion such that:

$$g(\mathbf{U}) \approx g(\mathbf{u}^*) + \nabla g(\mathbf{u}^*)(\mathbf{U} - \mathbf{u}^*) \tag{40}$$

where u^* is the expansion point and the gradient of $g(\mathbf{U})$ is defined as:

$$\nabla g(\mathbf{u}^*) = \left(\frac{\partial g(\mathbf{U})}{\partial U_1}, \frac{\partial g(\mathbf{U})}{\partial U_2}, \ldots, \frac{\partial g(\mathbf{U})}{\partial U_n}\right)\bigg|_{\mathbf{u}^*} \tag{41}$$

The determination of the reliability index involves identifying the shortest distance between the performance function and the origin of the U-space. This minimum distance point is referred to as the Most-Probable Point (MPP), and the distance is denoted as β. It is optimal to perform an expansion of the integration function on the MPP as it holds the highest probability density and contributes most significantly to the integration. Detailed insights into the derivation of the MPP search algorithm are comprehensively presented in [42]. The flow chart of MPP searching scheme is presented in Fig. 3.

The algorithm requires an initial guess of the MPP location denoted as $U_0 = (U_1^0, U_2^0, \ldots, U_m^0)$, where m represents the number of variables in
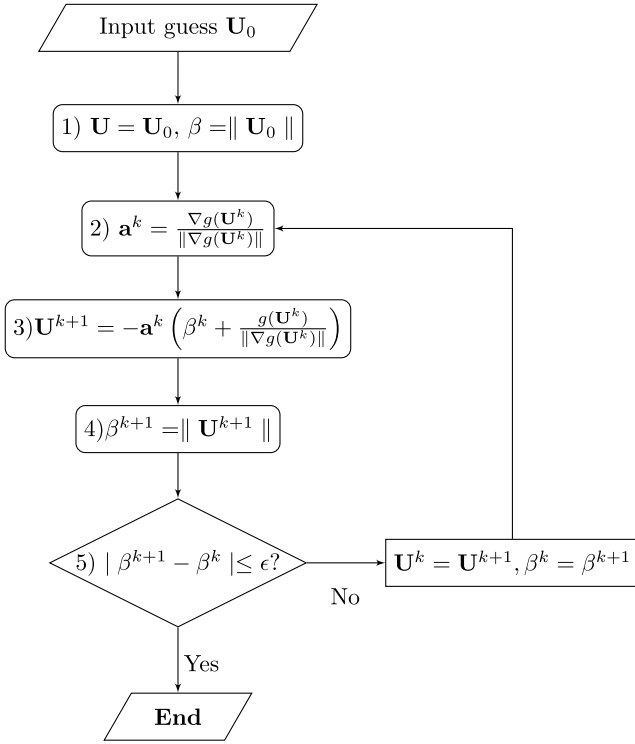
Fig. 3. MPP search algorithm.

the limit state function. Typically, the mean values of the variables are chosen as the initial guess, resulting in $U_0 = (0, 0, \ldots, 0)$ in the U-space.

In step (5) of the MPP search procedure, the convergence of the reliability index, β, is verified, with an error tolerance of $\epsilon = 1 \times 10^{-2}$ being used.

In step (3), it is essential to obtain the response of the Limit State Function (LSF), denoted as $g(\mathbf{U^k})$. As previously discussed, the DBEM serves as an effective tool for structural analysis and is thus employed to evaluate $g(\mathbf{U^k})$.

In step (2) involves the evaluation of the first-order derivative of the LSF. The gradient vector given in Eq. (41) can be evaluated by the DBEM-IDM formulation or DBEM-FDM formulation.

Once the MPP is identified, the probability of failure and reliability can be computed as follows:

$$P_R = 1 - P_F = 1 - \Phi(-\beta) = \Phi(\beta) \tag{42}$$

where Φ is the CDF of the standard normal distribution.

3. Numerical examples

In this section, two numerical examples examining the reliability of shallow shell structures were studied. The first example involves a shallow shell featuring a central hole and two cracks. The second example involves a more complicated geometry, incorporating multi-site damage. The results obtained from the reliability analysis were compared with those obtained from Monte Carlo Simulations (MCS) to verify the accuracy of the proposed approach.

3.1. Example 1: Reliability analysis of a shallow shell with centre hole and two cracks

A numerical example featuring a shallow shell with a central hole and two cracks subjected to a combination of membrane, bending, and uniform pressure loads was investigated. The material of the shell is Aluminium 2024-T4. The geometry of the shallow shell is shown

in Fig. 4(a). The shallow shell configuration includes a central hole characterized by a radius of r_1 and two cracks, each with a length of a. A deterministic initial crack length $a_0 = 5.08$ mm was considered. The curvature in the x-direction is denoted as κ_{11} and κ_{22} for y-direction. The shell thickness is defined as h, and the centre hole's position along the x-axis is denoted as b_1. The outer dimensions of the shell remain constant, with a width and length of 101.6 mm. The structural model was discretized using 32 quadratic elements on the outer boundaries, and 32 quadratic elements on the cracks and the central hole (with 8 elements allocated for each crack). Overall 64 DRM points were used and evenly distributed in the domain. The mesh of the boundary nodal points and DRM points is shown in Fig. 4(b). The shell, with a thickness of 2.54 mm, was subjected to tension, bending, and uniform domain pressure loads applied to the top and bottom boundaries. Simply supported boundary condition is applied long the sides of the shell such that $\phi_t = 0$ and $w_3 = 0$. The sensitivity of stress intensity factors was evaluated via both the DBEM-based IDM and the DBEM-based FDM.

The example is split into two parts. In the first part, a fracture reliability analysis was performed, with the fracture toughness taken as the failure criterion. The aim is to obtain a critical crack length. The second part involved a fatigue reliability assessment, utilizing the determined critical crack length to deduce the structure's service life.

3.1.1. Sensitivity of stress intensity factors

The parameters employed to assess the Sensitivity of the SIFs are detailed in Table 1. The evaluation of the sensitivity of the SIF with respect to each parameter were conducted using both the DBEM-FDM and DBEM-IDM and the crack surface displacements extrapolation technique (CSDE) at different crack length.

For the DBEM-FDM, the derivative can be evaluated using Eq. (36) with an optimal step size denoted as $\Delta Z'_g$ was determined through a convergence test. A range spanning from 0.5 to 10^{-6} was investigated. Larger step sizes influence the precision of the derivatives, while very small step sizes may introduce substantial rounding errors. The optimal step size was selected within the range of $\Delta Z'_g$ that yielded stable and accurate derivative solutions. The results of the convergence test for selecting an optimal step size are illustrated in Fig. 5. The data indicates that excessively large or small step sizes lead to significant errors in the results. An optimal balance between precision and stability was found within the range of $\Delta Z'_g = 10^{-2} - 10^{-4}$. Consequently, a step size of $\Delta Z'_g = 5 \times 10^{-2}$ was chosen for subsequent examples.

The growth of cracks was considered along the horizontal direction only. Geometric variables included the radius and the x-coordinate of the centre hole, with the aim to account for the potential impact of manufacturing uncertainties on SIFs. The variation in the x-coordinate of the centre hole introduces an antisymmetric in terms of the SIF in each crack tip. Therefore, the crack with a higher SIF was chosen and the corresponding derivatives were evaluated in each reliability analysis. The curvature varied more significantly in the y-direction, with a coefficient of variation COV set at 0.1. This choice is supported by previous literature [44], underlining its validity for the present study. Additionally, the uncertainties in the fracture toughness was introduced with a lognormal distribution characterized by a COV of 0.075, following established work [45]. The uncertainties in the geometrical parameters, loading and Pairs Law parameters were assigned according to the previous literature [46–50].

3.1.2. Reliability analysis

In the reliability analysis, it is essential to formulate the limit state function based on the structural resistance to a given loading condition, as introduced in Section 2.6. Subsequently, the reliability can be assessed using the FORM based on the limit state function. In this section, two reliability analyses were performed. The first analysis entails a limit state function formulated in terms of crack tip stress intensity factors and fracture toughness. This formulation ensures that
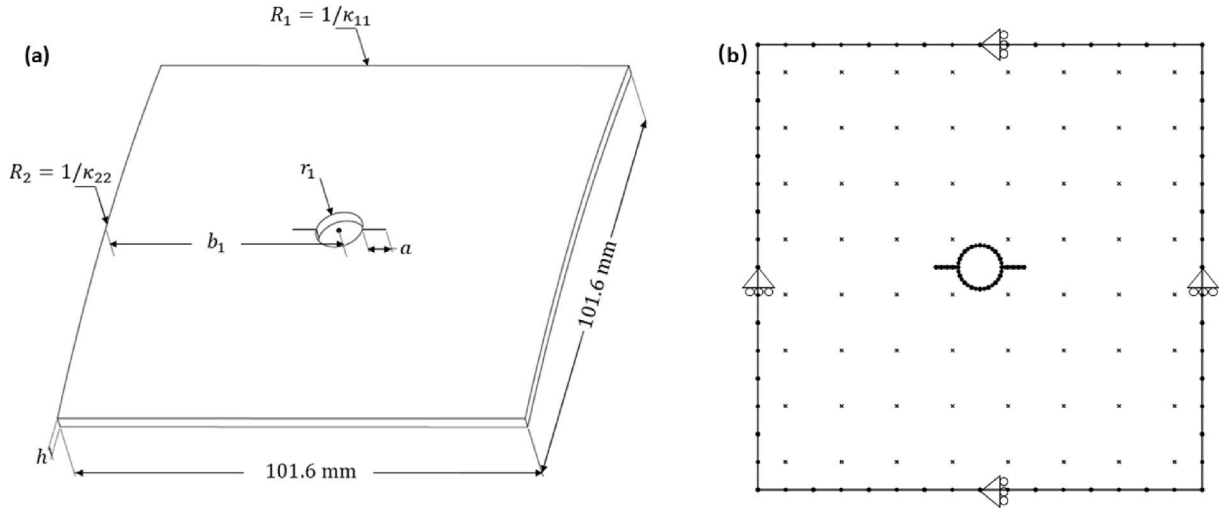
Fig. 4. (a): The geometry of the shallow shell structure used in the first numerical example. (b): The boundary element mesh of the shallow shell structure.
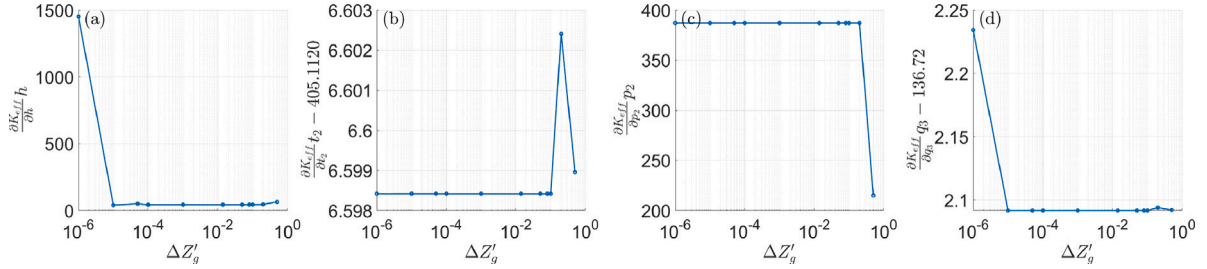

Fig. 5. A convergence test of derivatives using the Finite Difference Method (FDM) was conducted with respect to: (a) thickness, (b) membrane load, (c) bending load, and (d) domain pressure. The test investigated various ranges in the step size $\Delta Z'_g$, spanning from 0.5 to 10^{-6}. The objective of this test was to identify the step size that provides the best balance of numerical precision and stability for parameters.

Table 1
The design variables used in the reliability analyses.

Z_i	U_i	Parameter	Description	Distribution	Mean	COV
Z_1	U_1	r_1	Radius of the centre hole	Lognormal	5 mm	0.02
Z_2	U_2	b_1	x-coordinate of the centre hole	Lognormal	50.8 mm	0.02
Z_3	U_3	κ_{11}	Curvature in x direction	Lognormal	0.03 m^{-1}	0.1
Z_4	U_4	κ_{22}	Curvature in y direction	Lognormal	0.3 m^{-1}	0.1
Z_5	U_5	h	Thickness	Lognormal	2.54 mm	0.02
Z_6	U_6	t_2	Membrane traction	Lognormal	400 Nmm^{-1}	0.05
Z_7	U_7	p_2	Bending load	Lognormal	800 N	0.05
Z_8	U_8	q_3	Uniform domain load	Lognormal	0.15 MPa	0.05
Z_9	U_9	K_{IC}	Fracture toughness	Lognormal	36.12 MPa [43]	0.075
Z_{10}	U_{10}	C_0	Paris law Constant	Lognormal	$1.42 \times 10^{-11} \frac{\text{m/cycle}}{(\text{MPa}\sqrt{m})^{m_p}}$	0.02
Z_{11}	U_{11}	m_p	Paris law exponent	Lognormal	3.59	0.02

the crack tip SIF remains below the fracture toughness threshold. It is anticipated that the reliability decreases with an increase in the crack size. This reliability analysis is coupled with the probability of detection to establish a permissible crack size, denoted as a_t, while satisfying the given safety criteria. The second reliability analysis was performed with a limit state function defined by the service life of the structure and the cumulative loading cycles required to reach the determined permissible crack size a_t from the first reliability analysis. This analysis accommodates uncertainties inherent in crack growth parameters, which play a vital role in determining an appropriate inspection service interval.

3.1.3. Fracture reliability analysis

The first analysis entails a limit state function formulated in terms of crack tip stress intensity factors and fracture toughness. A suitable LSF in terms of the failure criteria used in this work is [51]:

$$g(\mathbf{Z}) = K_{IC} - K_{eff}(\mathbf{X}) \tag{43}$$

where K_{IC} denotes the fracture toughness and K_{eff} denotes the effective stress intensity factor. The vector $\mathbf{Z}$ comprises the design variables that exert influence on the value of $g(\mathbf{Z})$, represented as $\mathbf{Z} = (r_1, b_1, \kappa_{11}, \kappa_{22}, h, t_2, p_2, q_3, K_{IC})$, while $\mathbf{X}$ includes the design variables within $\mathbf{Z}$ excluding the fracture toughness, expressed as $\mathbf{X} = (r_1, b_1, \kappa_{11}, \kappa_{22}, h, t_2, p_2, q_3)$. The distributions of these design variables are detailed in Table 1. The derivatives of K_{eff} with respect to the design variables were evaluated using the formulation introduced in Section 2.4.

The derivatives of the nodal coordinates with respect to Z_i can be computed analytically using the DBEM-IDM. Among these variables, Z_1 to Z_4 are geometrical variables and curvatures, and their sensitivities were analytically evaluated using the DBEM-IDM. Conversely, the sensitivities with respect to non-geometrical variables Z_5 to Z_{11} were evaluated using the DBEM-FDM with a step size of $\Delta Z'_g = 5 \times 10^{-2}$. The reliability analysis was carried out over a range of crack lengths. It is
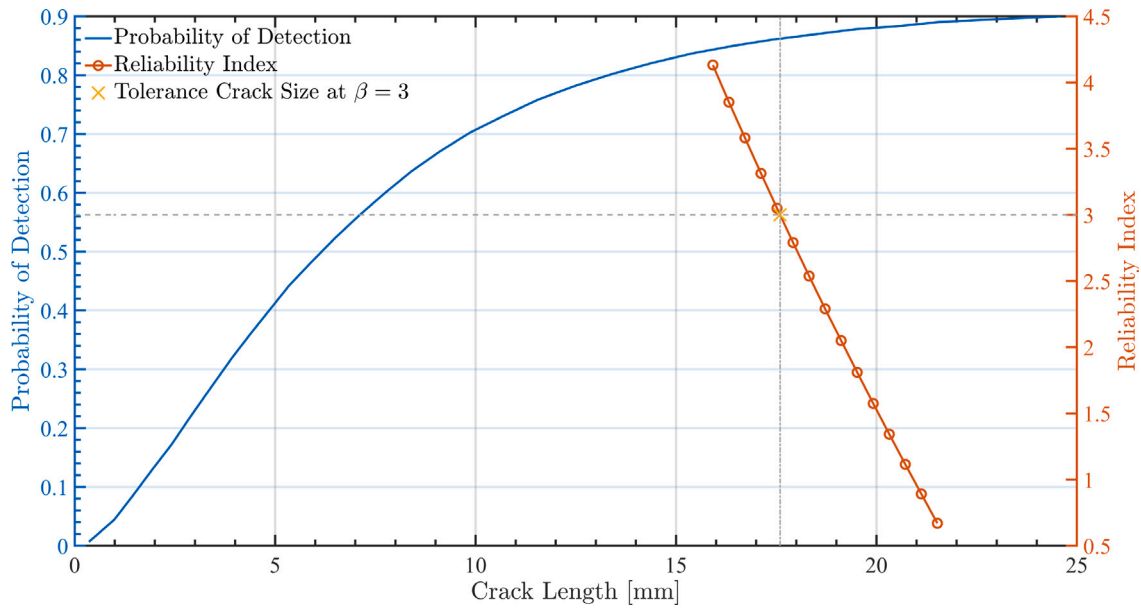
Fig. 6. The graph shows the reliability index with variations in crack length (shown on the right y-axis). Additionally, an illustration of the probability of detection obtained from handheld eddy-current inspection is presented against the crack size (displayed on the left y-axis) [53]. The tolerable crack size was determined at a reliability index of $\beta = 3$, which corresponds to a crack length of 17.6 mm, as indicated by the cross on the graph. Notably, the corresponding probability of detection is measured at 86.3%.

anticipated that as the crack propagates, the structure's reliability will decrease.

In the context of tolerance design and considering routine inspection, the tolerable crack size should be chosen to be both below the critical crack size according to a safety criterion while remaining sufficiently large to be detectable by inspection techniques [52]. In the reliability analysis, the tolerable crack size can be determined by a required reliability index β, which varies based on the specific application of the structure. Prescribed reliability indices can often be found in standard data sheets, such as the Eurocode - Basis of Structural Design. In this example, targeting reliability of $\beta = 3$ was selected, which is within the range of minimum reliability indices recommended for structures under fatigue limit state conditions.

The results of the reliability index with varying crack lengths are displayed in Fig. 6, alongside by the probability of detection data of a handheld Eddy-Current inspection [53]. As anticipated, the reliability index displayed a decreasing trend as the crack size increased. The tolerable crack size $a_t = 17.6$ mm was determined to correspond to a reliability index of $\beta = 3$. At this chosen crack size, the Probability of Detection (POD) is of 86.3%, which is considered within an acceptable range. It is worth noting that in practical applications, the selection of targeting reliability and desired POD should encompass additional considerations, including factors such as inspection conditions and risk acceptance levels. For instance, components associated with potential catastrophic failure consequences should have a stricter tolerance design.

3.1.4. Fatigue reliability assessment

The second reliability analysis was performed with a limit state function defined by the service life of the structure and the cumulative loading cycles required to reach the determined permissible crack size a_t from the first reliability analysis. For the fatigue crack growth reliability analysis, the limit state function is defined as:

$$g(\mathbf{Z}) = N(\mathbf{Z}) - N_s \tag{44}$$

where $N(\mathbf{Z})$ represents the number of cycles required to reach the tolerable crack length a_t, while N_s denotes the service life in terms of the loading cycles experienced by the structure during its service duration. The set of uncertainties influencing fatigue crack growth is denoted by $\mathbf{Z}$, including variables $\mathbf{Z} = (r_1, b_1, \kappa_{11}, \kappa_{22}, h, t_2, p_2, q_3, C, m)$.

The precise distribution of these uncertainties can be found in Table 1. It is important to note that the Paris law constants C and m are typically established through experimental assessment under specific loading conditions. Consequently, a dependency between the parameters linked to the loading situation and the Paris law constants was considered.

An important assumption when performing the FORM is that the random variables are assumed to be mutually independent. This analysis incorporates two limit state functions to isolate and examine the impact of loading conditions and Paris law constants. The first limit state function introduces uncertainties solely in loading conditions while treating the Paris law constants as deterministic. Conversely, the second limit state function introduces uncertainties in the Paris law constants while maintaining the loadings at their mean values in a deterministic fashion. For both scenarios, it is reasonable to anticipate that shorter service life durations would correspond to higher structural reliability. Two limit state functions were formulated as follows:

- Limit state function I:

$$g(\mathbf{Z_1}) = N(\mathbf{Z_1}) - N_s, \qquad \text{where } \mathbf{Z_1} = (r_1, b_1, \kappa_{11}, \kappa_{22}, h, t_2, p_2, q_3) \tag{45}$$

- Limit state function II:

$$g(\mathbf{Z_2}) = N(\mathbf{Z_2}) - N_s, \qquad \text{where } \mathbf{Z_2} = (r_1, b_1, \kappa_{11}, \kappa_{22}, h, C_0, m) \tag{46}$$

The fatigue life N of the structure was approximated by the Paris Law such that:

$$N = \int_{a_0}^{a_t} \frac{1}{C(\Delta K_{eff})^m} \, da \tag{47}$$

where $C = \frac{C_0}{(1-R)^{m(1-\gamma)}}$ and $\Delta K_{eff} = (1 - R)K_{eff}$. The stress ratio is set at $R = 0.1$ and $\gamma = 0.68$ in this example. The derivatives of the fatigue life N can be derived in terms of the K_{eff}. This results in the following expressions for the derivatives of N with respect to the design variables:

$$N_{,g} = \int_{a_0}^{a_t} \frac{-m}{C} (\Delta K_{eff})^{-m-1} \Delta K_{eff,g} \, da \tag{48}$$

The derivatives of the effective SIF can be computed using $\Delta K_{eff,g} = (1 - R)K_{eff,g}$ with a constant stress ratio R. The integration involved
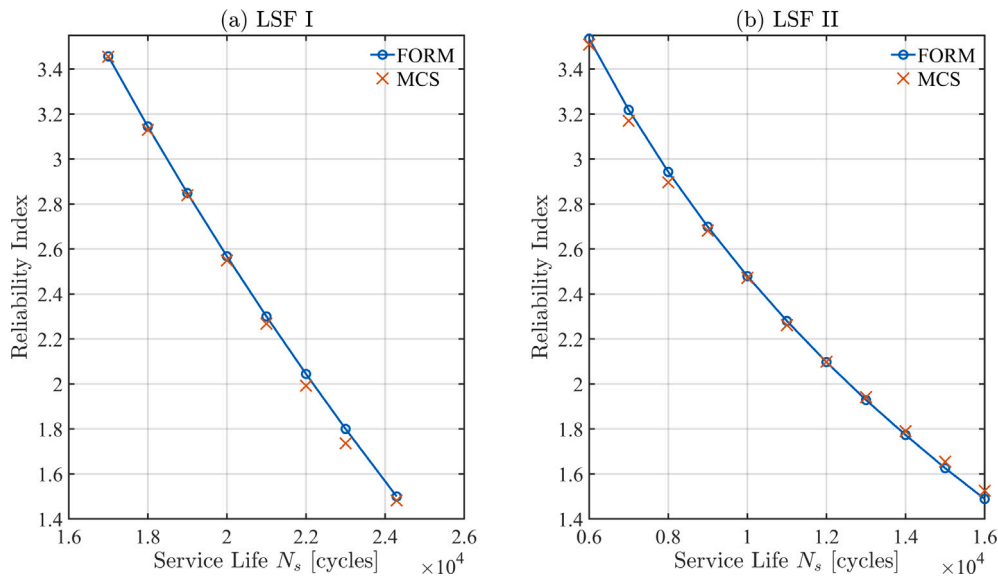
Fig. 7. The reliability index against the number of loading cycles to which the structure has been exposed (service life) is shown for LSF I (a) and LSF II (b). The results of the Monte Carlo Simulation are illustrated for both LSFs. The highest difference observed in LSF I is at the value of 3.76% at 23 000 cycles, while in LSF II it is found at 2.40% at 16 000 cycles.

in Eqs. (47), (48) was approximated using trapezoidal numerical integration with evenly spaced point from $a_0 - a_t$. This same approach was employed to evaluate the sensitivity of N with respect to the curvature. The results of the two limit state functions are presented in Fig. 7 Both sets of results were compared against MCS consisting of $N_{mcs} = 40,000$ simulations to validate the accuracy of the proposed IDM formulations and their integration with FORM. The probability of failure from the MCS was determined by

$$P_{F,MCS} = \frac{n_{N<N_s}}{n_{MCS}} \tag{49}$$

It is worth noting that the number of MCS simulations was determined such that the mean and standard deviation of the distribution of N_s obtained from MCS are converged with a difference of 0.1%.

The accuracy achieved an acceptable level, with a maximum difference of 3.67% for LSF I at 23 000 cycles and 2.40% for LSF II at 16 000 cycles. Notably, FORM demonstrated a high level of accuracy, particularly for high-reliability indexes that engineers commonly employ.

It is evident that when identical uncertainties in geometrical parameters are considered, the uncertainties in Paris law constants exert a more significant impact on the service life and reliability analysis as shorter service life are observed for LSF II given the same β compare to LSF I. This observation underscores the need for more frequent inspections due to the variations in Paris law constants. The outcomes presented above illustrate the combined influence of parameters. To separate the effects of individual parameters, a parametric analysis was conducted, where a single parameter was treated as uncertain in the reliability analysis while the remaining parameters as deterministic. The parametric test was separated into three groups: geometrical parameters, loading conditions, and Paris law constants.

Fig. 8 demonstrate the impact of uncertainties in geometrical parameters, it is evident that for a given reliability index, the curvature in the x-direction κ_1 leads to the longest service life and has a minor effect on reliability. This aligns with expectations as x-direction curvature is smaller and thus less influential compared to y-direction curvature. Conversely, uncertainties in the thickness exhibited a more pronounced impact on reliability. This is evident from the fact that the same reliability index corresponds to a shorter service life along the thickness line compared to other geometrical parameters.

The results for the influence of the loading conditions are shown in Fig. 9. The result shows that the membrane traction force t_2 has a

higher influence in determining a suitable service life while the domain pressure load has a minor effect on the service life.

In terms of Paris Law constants, Fig. 10 shows that the Paris Law exponential term m as the only random variable results in the shortest service life among all parameters. This is within the expectation that the Paris Law exponent poses the largest impact on the reliability and hence service life as the number of cycles is highly dependent on the magnitude of the exponent.

The remaining parameters yield a relatively consistent range of service life when modelled as the only uncertainty. This highlights that service life is significantly impacted by thickness, membrane traction, and the Paris Law exponential term. Hence, design efforts should focus on accurately determining the variation of these parameters to achieve a longer service life.

A sensitivity test of the reliability index concerning the coefficient of variation (COV) was conducted. The uncertainties associated with geometrical parameters are conventionally standardized by the manufacturer with the same level of uncertainty (COV) for all parameters. The same principle applies to the loading parameters and Paris law constants, resulting in equal levels of uncertainty for all. This approach aims to investigate uncertainties across three distinct parameter categories: geometrical, loading, and Paris law constants. By increasing the COV within these three parameter groups, ranging from 0.01 to 0.05, the probability of failure increases. The results of the sensitivity test are shown in Fig. 11. The findings underscore that a higher level of uncertainty in parameters corresponds to a higher failure probability, as expected. The impact of COV variations in geometrical and loading parameters has relatively minor effects on reliability, resulting in a 0.25% increase in the probability of failure for the loading parameter and a 1% increase for the geometrical parameters. In contrast, variation in the uncertainty levels of the Paris law constants significantly increases the probability of failure. It is necessary to determine the variation in the Paris law constants in a more accurate way to maintain low COV in the uncertainty, hence decreasing the probability of failure.

3.2. Example 2: Fatigue reliability analysis of multi-site damage in a shallow shell

A second numerical example was investigated, involving the assessment of fatigue reliability concerning a cylindrical shallow shell structure with multiple site damage. The geometry of the structure is
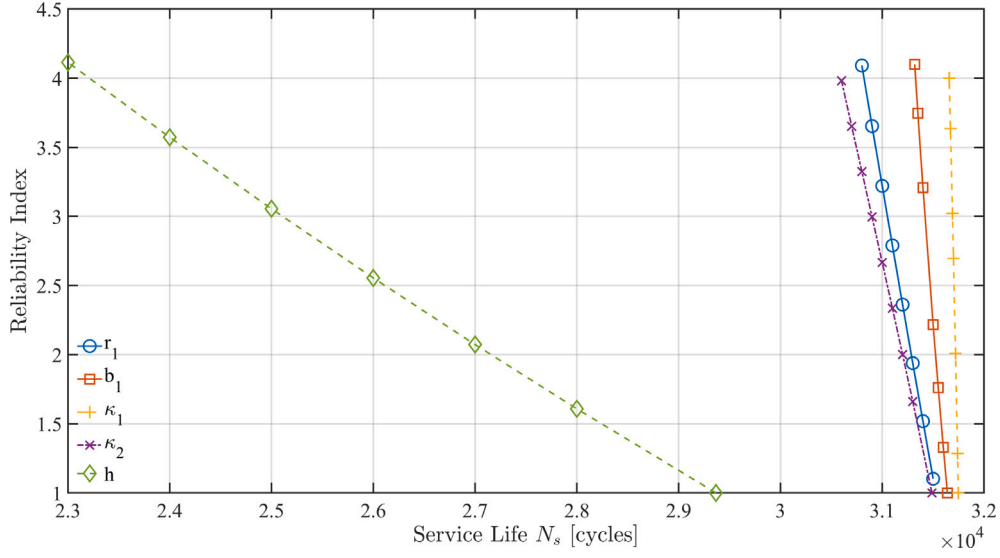
Fig. 8. The parametric analysis investigated the influence of uncertainties in the geometrical parameters on the structure's reliability.
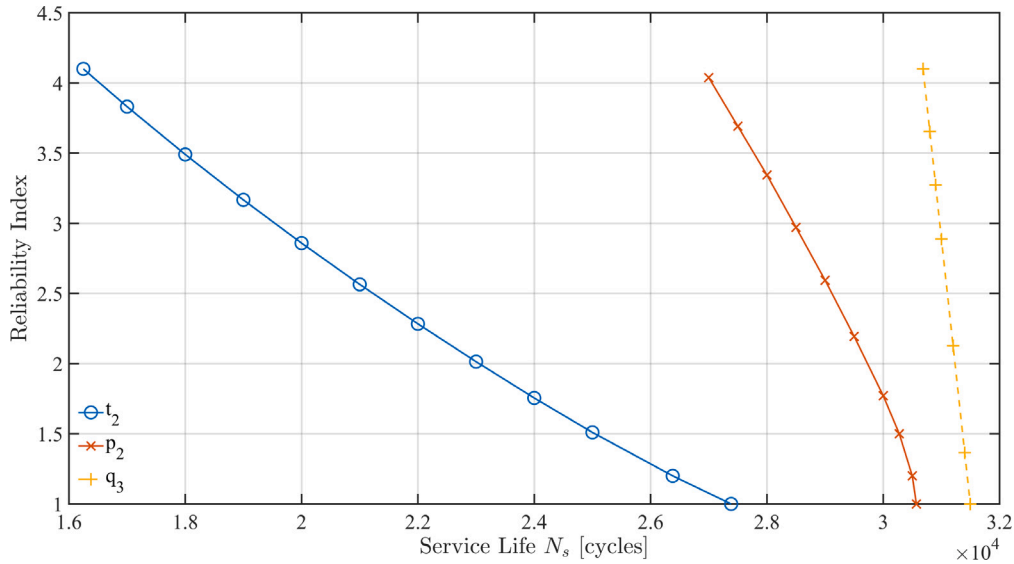

Fig. 9. The Parametric analysis of the uncertainties in the loading parameters to the reliability of the structure.

presented in Fig. 12. The geometry comprises three holes featuring two cracks each extending from opposing sides of each hole. The cracked section of the shell is denoted as region A, and specific structural dimensions are outlined in Table 2. The initial crack lengths a_0^i in C1–C6 were treated as an uncertainty, where $i \in [1, 6]$. The shell is made of Aluminium 2024-T3, with Young's modulus of $E = 73.78$ GPa and a Poisson's ratio of $v = 0.33$. The structure was discretized using 30 quadratic elements on the shell's outer boundaries. The same boundary conditions were applied as in the previous example. Additionally, 8 quadratic elements were allocated to each hole, with 4 quadratic elements each on the upper and lower surfaces of the cracks. Overall, 102 quadratic elements were used. 70 DRM points were used and were uniformly distributed throughout the domain (see Fig. 13).

In this example, the geometrical parameters remained constant except for the initial crack lengths at cracks $C1$ to $C6$, where each of the crack lengths are treated as an uncertainty. The reliability analysis was conducted with varying curvature in the y direction ($\kappa_{11} = 0$, $\kappa_{22} = \kappa$). The initial length of each crack is allowed to have different lengths.

All cracks were grown to a final length of $a_f = 8$ mm, and the fatigue life of the structure is defined as the number of cycles required for the crack to reach this length. The reliability was evaluated on the crack with minimum fatigue life among all crack tips.

Four reliability analyses were conducted with curvature in y-direction taking the value of $\kappa = (1.0E{-}14, 0.01, 0.05, 0.1)$ m^{-1} to investigate the effect of curvature on the overall reliability, where the case of $\kappa = 1.0E{-}14$ m^{-1}, the shell can be considered as a plate. The limit state function can be written as:

$$g(a_0^i, p, C, m, N_s) = N(a_0^i, p, C, m) - N_s \quad (50)$$

where $i \in [1, 6]$ for uncertainty in the initial crack length of crack $C1 - C6$. The derivatives of the fatigue life N can be found by differentiating the integral equation using trapezoidal numerical integration. The integration in Eq. (47) can be approximated by a trapezoidal rule with evenly spaced points such that:

$$N = \int_{a_0}^{a_f} f(a)da \approx \frac{a_f - a_0}{2N} \left[f(a_0) + 2f(a_1) + \cdots + 2f(a_N) + f(a_f) \right] \quad (51)$$
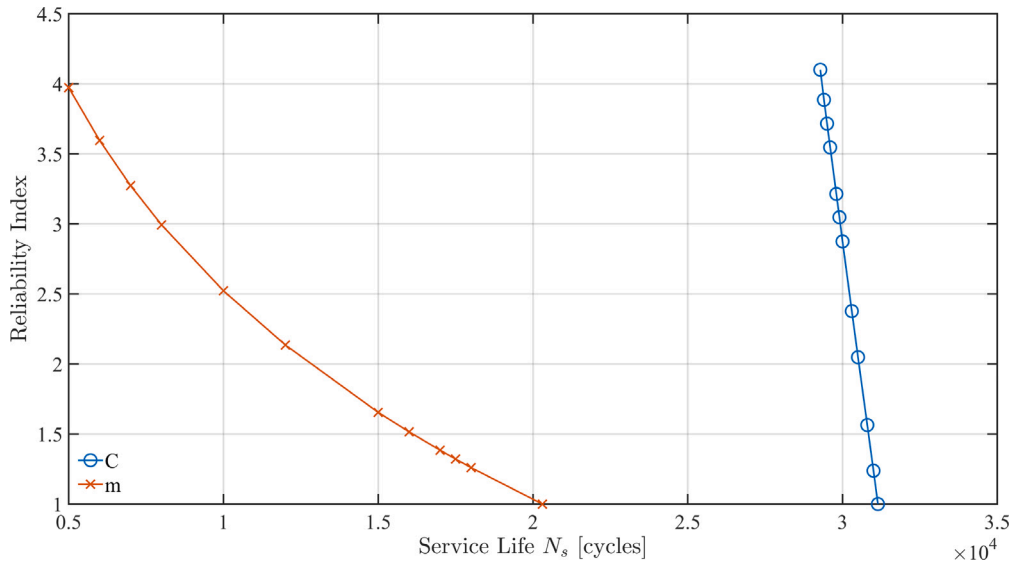
Fig. 10. The Parametric analysis of the uncertainties in the Paris law constants to the reliability of the structure.
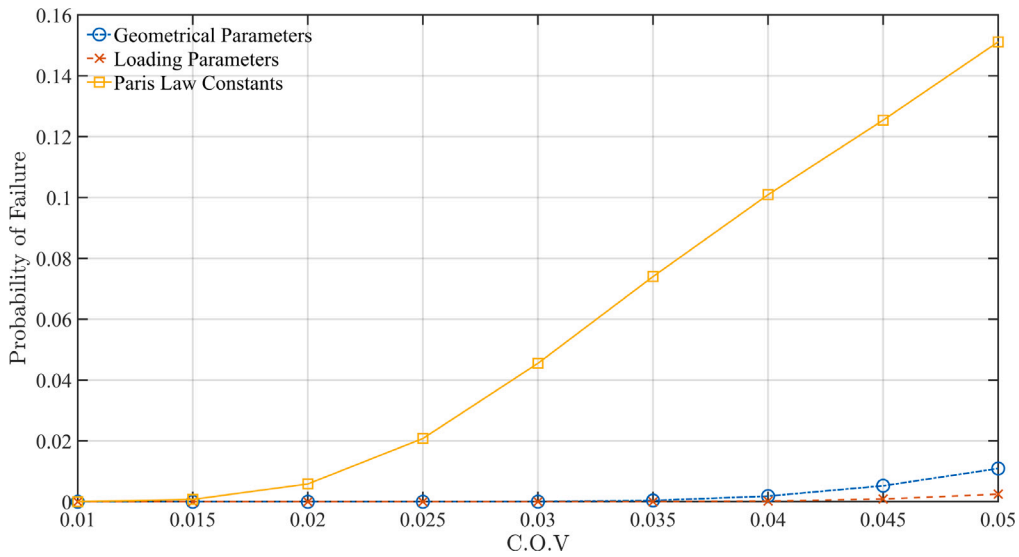

Fig. 11. The parametric analysis of the combined effect of geometrical variables, loading parameters and Paris Law constants respectively with the same level of COV in the parameter.

Table 2
Geometrical factors and uncertainties present in example 2. The uncertainty considered in this example includes the initial crack length in each of the six different crack positions, loading conditions and Pari's law constants.

| Parameter	Description	Distribution	Mean	COV
W	Width of the shell	Deterministic	160 mm	
L	Length of the shell	Deterministic	300 mm	
κ	Curvature in y direction	Deterministic	Variable	
h	Thickness	Deterministic	2 mm	
D	Diameter of the holes	Deterministic	3 mm	
ΔL	Distance between the holes	Deterministic	30 mm	
a_0^1	Initial crack length in C1	Lognormal	3.5 mm	0.05
a_0^2	Initial crack length in C2	Lognormal	3.5 mm	0.05
a_0^3	Initial crack length in C3	Lognormal	3.5 mm	0.05
a_0^4	Initial crack length in C4	Lognormal	3.5 mm	0.05
a_0^5	Initial crack length in C5	Lognormal	3.5 mm	0.05
a_0^6	Initial crack length in C6	Lognormal	3.5 mm	0.05
p	Pressure loading	Lognormal	0.05 MPa	0.05
C	Paris Law constant	Lognormal	$2.839 \times 10^{-12} \frac{\text{m/cycle}}{(\text{MPa}\sqrt{m})^{m_p}}$	0.05
m_p	Paris Law exponent	Lognormal	4.6	0.02
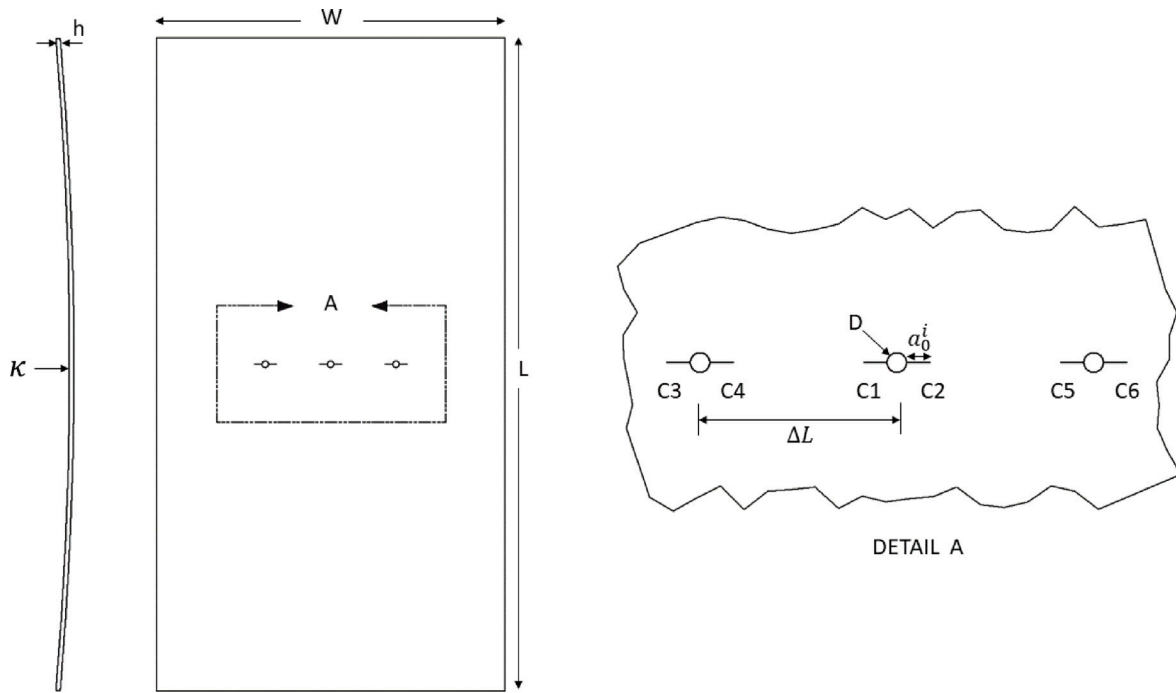
Fig. 12. The geometry of the shallow shell used in the second reliability analysis. The geometry comprises three holes featuring two cracks extending from opposing sides of each hole. The cracked section is denoted as region A.
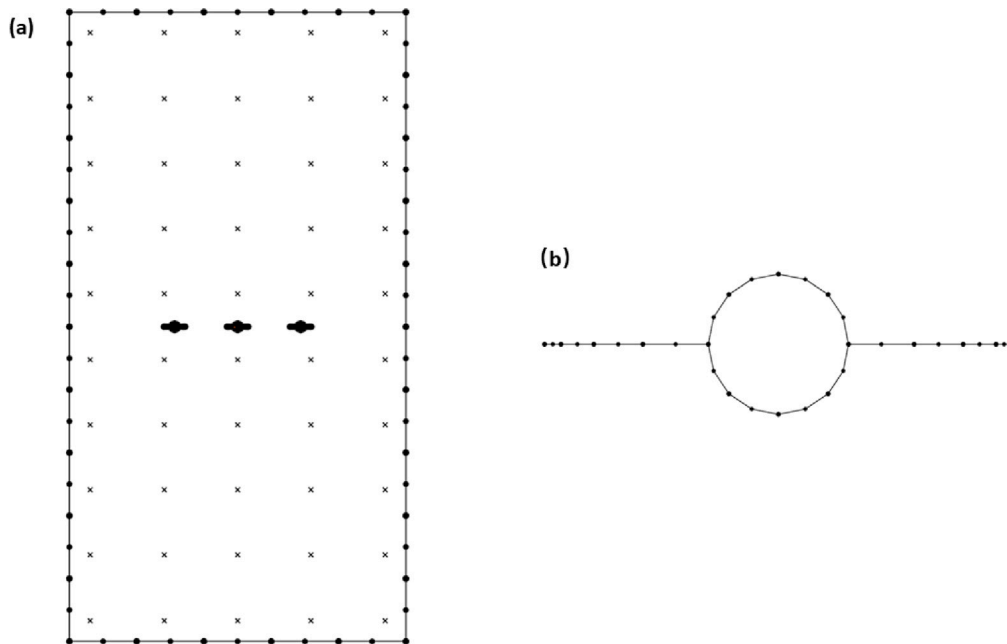

Fig. 13. (a): The boundary element mesh of the shallow shell used in the second reliability analysis. (b): The mesh on the centre hole and crack. Only the mesh of the middle hole is shown here, the rest of the holes were meshed in the same way.

where $f(a) = \frac{1}{C(\Delta K_{eff}(a))^m}$. The derivatives with respect to the initial crack length can be found:

$$N_{,a_0} \approx \frac{a_f - a_0}{2N} \left[f'(a_0) + 2f'(a_1) + \cdots + 2f'(a_N) + f'(a_f) \right]$$
$$- \frac{1}{2N} \left[f(a_0) + 2f(a_1) + \cdots + 2f(a_N) + f(a_f) \right] \tag{52}$$

The derivatives of the fatigue life N at crack tip j with respect to change in initial crack size a_0^i were calculated at each MPP iteration, using Eq. (52) for $j = i$ and Eq. (48) for $j \neq i$. It is expected that with increasing curvature, the structure exhibits higher resistance to crack

propagation, consequently leading to longer fatigue life. The IDM-based FORM was used and the results of which were then compared with those of MCS.

Overall, 1×10^5 MCS iterations were conducted for each curvature value, and the results derived from both FORM and MCS are shown in Fig. 14. The number of required MCS was determined in the same way as mentioned in the previous section. The outcomes generated through the FORM approach exhibit high consistency with the MCS results, with the maximum deviation of 3.49% recorded at $\beta = 2.23$ when $\kappa = 0.05$. The results show a larger error at a smaller reliability
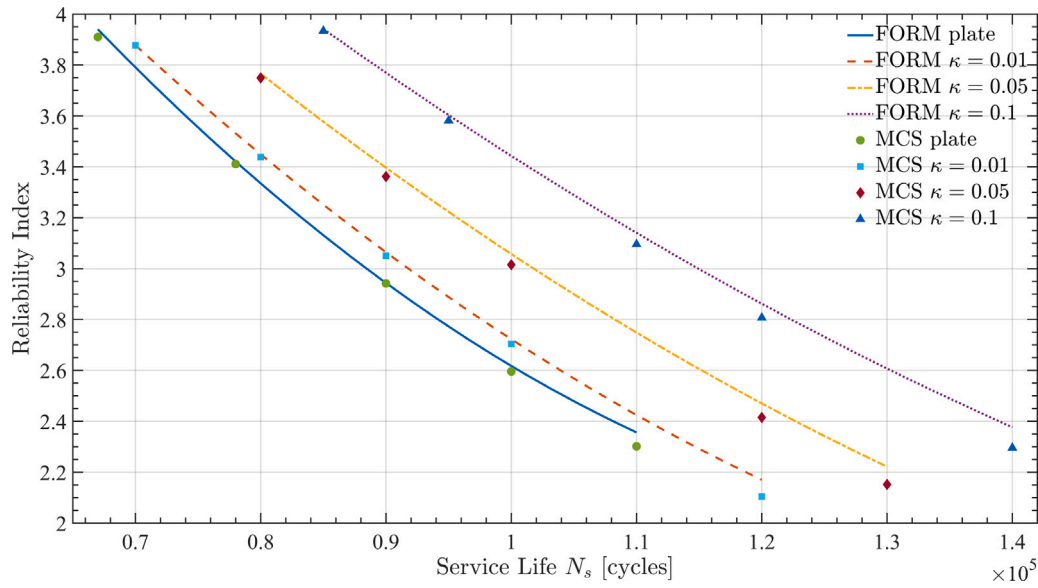
Fig. 14. The reliability index concerning the structure's service life, influenced by different curvatures of the shell structure is shown in the figure. To validate the accuracy of the findings, the results of the Monte Carlo Simulation are included for comparison.

index. The reliability index illustrates substantial sensitivity to changes in shell curvature. Specifically, as curvature increases, longer service life can be achieved while maintaining the same reliability index, thereby reducing the probability of failure. The results agreed with the expectation. In average, four iterations in average for obtaining the converged reliability index. The computational time required to evaluate the FORM results for one curvature is 7.58×10^4 s. The computational time required for one DBEM simulation is 626.4 s. The total amount of computational time required by the MCS is, therefore, 6.26×10^7 s. The FORM requires significantly less computational effort while maintaining high accuracy. This shows the robustness and efficiency of the proposed formulation.

The Omission sensitivity factor has been used in FORM to provide information about the sensitivity of parameters and the impact of uncertainties on failure probability [54]. The Omission factor γ can be evaluated as:

$$\gamma_j = \frac{\beta - \alpha_j u_j}{\beta \sqrt{1 - \alpha_j^2}} \tag{53}$$

where j denotes the index representing the number of design parameters considered in the reliability analysis. The term α refers to the gradient vector determined in step 2 of Fig. 3, while u represents the design point vector in the standard normal space. To illustrate, the Omission Sensitivity Factors were assessed at the design point where $\kappa = 0.1$, with the outcomes presented in Fig. 15 considering different service life.

A parameter whose corresponding Omission factor approaches unity suggests that it may be considered deterministic. The pressure load and Paris law constants exert a more significant influence on the failure probability, whereas the effect of varying initial crack sizes is minimal. Notably, with the initial crack size at $C2$, a comparatively larger Omission factor is observed. This implies that the initial crack sizes could be treated as a deterministic variable, while quantifying the uncertainties in pressure load and Paris law constants can substantially enhance structural reliability.

It is worth noting that in both numerical examples in this section, the difference between the FORM and MCS can be reduced by using the SORM, which approximates the LSF with a second-order Taylor expansion. This can significantly improve the accuracy of the estimated reliability index, especially for problems with highly nonlinear LSFs. When dealing with higher-dimensional problems that incorporate

multiple uncertainties, there is a marked increase in the number of derivatives that need to be computed. This increase can lead to substantial computational challenges. In such situations, the application of MCS with surrogate modelling is preferential to mitigate these computational demands. This combination effectively reduces the overall computational burden while maintaining accuracy in the analysis of more complex, multi-variable systems.

4. Conclusion

This paper introduces a novel methodology for performing reliability analyses of fatigue life through the newly developed Dual Boundary Element Method-based Implicit Differentiation Method (DBEM-IDM) for shallow shell structures. The study has introduced DBEM-based formulations that enable the evaluation of stress intensity factor and fatigue lifetime sensitivities within shallow shell structures, concerning variations in geometrical variables and curvature. The proposed methodology holds the potential to significantly advance current capabilities in predicting the reliability of such structures under fatigue conditions, thereby enhancing their overall design and assessment processes.

The IDM formulations were derived by directly differentiating the BEM equations and were integrated with First Order Reliability Analysis (FORM) to assess the reliability index of shallow shell structures featuring multiple cracks, thus estimating the probability of failure. FORM offers a distinct advantage by significantly reducing computational demands while maintaining accuracy compared to the Monte Carlo Simulation (MCS). In order to demonstrate the effectiveness of the proposed approach, two numerical examples were presented. In the first example, a shallow shell featuring a central hole and crack, subjected to membrane, bending, and uniform pressure loads, was investigated. The fracture reliability analysis was conducted and considered a limit state function formulated in terms of effective stress intensity factor K_{eff} and fracture toughness. The obtained reliability index results were coupled with the probability of detection from eddy current inspections, aiding in determining a critical crack length that would satisfy reliability requirements while allowing for inspectability.

Additionally, fatigue reliability assessments were carried out through limit state functions expressed in terms of fatigue life cycles. Two limit state functions were analysed to separate the impacts of loading conditions and Paris law constants. The results obtained from
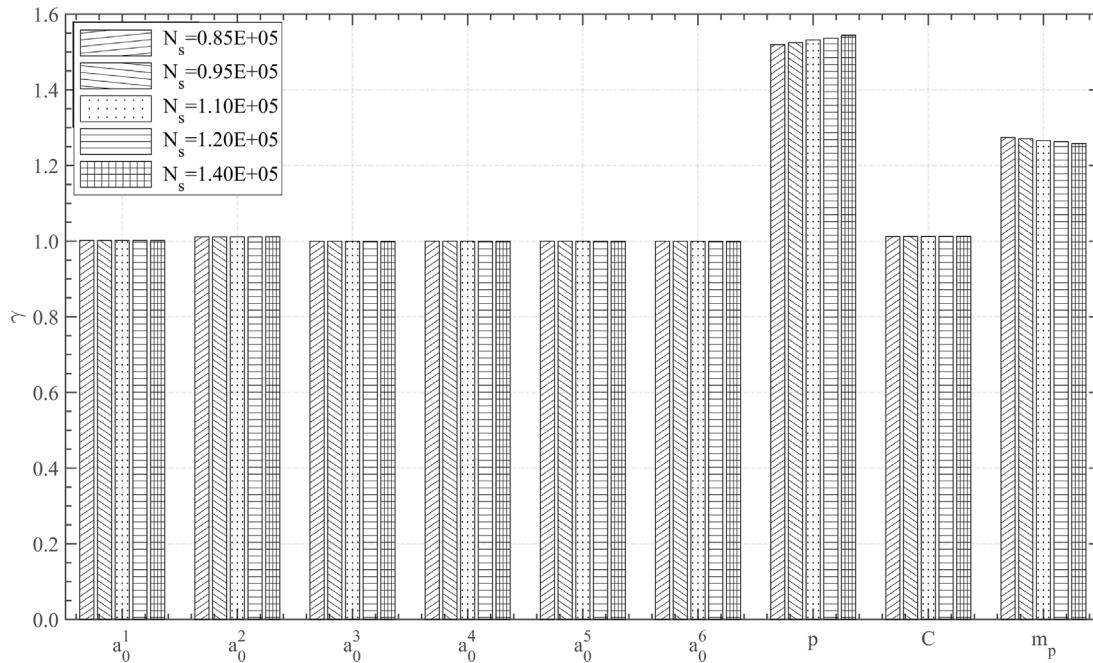
Fig. 15. Omission sensitivity factors for the case when $\kappa = 0.1$ with various service life.

FORM were benchmarked against the results obtained from 40,000 MCS iterations, showing a maximum difference of only 3.67%. Furthermore, a parametric analysis was conducted on each design variable to identify the most influential factors on overall structural reliability. It was determined that thickness, membrane traction, and the Paris Law exponential term have a significant influence on service life, underscoring the need for precise determination of these parameters to achieve extended service life. The investigation further encompassed the influence of the coefficient of variation (COV). It was discovered that uncertainties associated with Paris law constants exerted a more substantial influence, prompting the need for enhanced precision in determining these constants to improve structural reliability and reduce the probability of failure.

A second numerical example investigated the fatigue reliability assessment of a cylindrical shallow shell structure with multiple-site damage, featuring six cracks with the initial crack length as variables. Varied curvature of the shell structure was used to investigate the effect of curvature on the reliability of the structure. Comparison of FORM results with those obtained from 1×10^5 MCS iterations revealed a maximum difference of only 3.49%. The computational time required for evaluating the reliability index for one curvature via FORM was around 7.58×10^4 s while achieving a converged distribution for the limit state function through MCS required a substantial 6.26×10^7 s. This comparison demonstrates the substantial efficiency of the IDM-based FORM in estimating the structural reliability index, particularly for higher-dimensional problems involving multiple random design variables, a scenario that typically requires a large amount of MCS. The proposed method shows good agreement with the MCS, demonstrating that the numerical FORM used in this study is valid. It is worth noting that the numerical examples presented in this study were assigned with a postulated initial crack size in either a deterministic way or with uncertainties. In many real-world scenarios, determining the actual initial flaw size with high precision can be both challenging and economically expensive. This underscores the application of the concept of the Equivalent Initial Flaw Size (EIFS) such that it provides a starting point for the crack propagation model.

The FORM is accurate and efficient for low-dimensional problems. While requiring evaluation of derivatives, this efficiency can be reduced when comes across to higher-dimensional problems. The accuracy of results achieved through FORM depends on the linearity or near-linearity

of the limit state function within the variable space. To improve the precision of derived reliability indices, the application of the Second-Order Reliability Method (SORM) is usually employed. This method involves approximating the limit state function using a second-order Taylor expansion, with an associated increase in computational complexity due to the inclusion of second-order derivatives. However, it is worth noting that FORM has demonstrated both efficiency and accuracy across a broad spectrum of structural problems. Furthermore, FORM has exhibited significant accuracy in the context of static structures, underlining its robustness for these scenarios.

The proposed IDM formulation has limited application on reliability analysis of straight propagating crack, where in the consideration of changing direction of crack propagation, the derivatives with respect to local elemental coordinate should be derived. Future work will focus on deriving and applying IDM to the reliability analysis of crack propagation with different orientation and assembled structures, such as aircraft fuselages. Additionally, investigations into the impact of fatigue crack growth on the reliability of assembled plate-shallow shell structures will be conducted, contributing to a more comprehensive understanding of fracture problems in engineering design.

CRediT authorship contribution statement

Mengke Zhuang: Writing – review & editing, Writing – original draft, Visualization, Validation, Software, Methodology, Investigation, Formal analysis. **Llewellyn Morse:** Writing – review & editing, Software, Resources, Methodology, Conceptualization. **Zahra Sharif Khodaei:** Writing – review & editing, Supervision, Conceptualization. **M.H. Aliabadi:** Writing – review & editing, Supervision, Methodology, Conceptualization.

Declaration of competing interest

The authors declare that they have no known competing financial interests or personal relationships that could have appeared to influence the work reported in this paper.

Data availability

Data will be made available on request.

Acknowledgement

All authors approved the version of the manuscript to be published.

Appendix

The derivatives of the Stress Intensity Factors (SIFs) with respect to geometry variables Z_g are given in Section 2.4. A similar approach was used for deriving the derivatives of SIFs with respect to curvature Z_ρ and thickness Z_h. The formulations are given in this section.

For simplification, denote:

$$T_\kappa = [1 + \frac{h}{4}(\frac{1}{R_1} + \frac{1}{R_2})]^{-1} = [1 + \frac{h}{4}(\kappa_{11} + \kappa_{22})]^{-1} \tag{54}$$

and its derivative:

$$T_{\kappa,\rho} = -\left[1 + \frac{h}{4}(\kappa_{11} + \kappa_{22})\right]^{-2} \frac{h}{4}(\kappa_{11,\rho} + \kappa_{22,\rho}) = -\frac{T_\kappa^2 h}{4}(\kappa_{11,\rho} + \kappa_{22,\rho}) \tag{55}$$

The derivatives of the maximum SIF can be found by:

$$K_{I,\rho}^{max} = \left(\frac{1}{h}K_{1\ m,\rho} + \frac{6}{h^2}K_{1b,\rho}\right)T_\kappa + \left(\frac{1}{h}K_{1m} + \frac{6}{h^2}K_{1b}\right)T_{\kappa,\rho}$$

$$K_{II,\rho}^{max} = \left(\frac{1}{h}K_{2\ m,\rho} + \frac{6}{h^2}K_{2b,\rho}\right)T_\kappa + \left(\frac{1}{h}K_{2m} + \frac{6}{h^2}K_{2b}\right)T_{\kappa,\rho} \tag{56}$$

$$K_{III,\rho}^{max} = \left(\frac{3}{2h}K_{3b,\rho}\right)T_\kappa + \left(\frac{3}{2h}K_{3b}\right)T_{\kappa,\rho}$$

Similarly, the derivative of T_κ is:

$$T_{\kappa,h} = \frac{\partial T_\kappa}{\partial h} = -\left[1 + \frac{h}{4}(\kappa_{11} + \kappa_{22})\right]^{-2} \frac{1}{4}(\kappa_{11} + \kappa_{22}) = -\frac{T_\kappa^2}{4}(\kappa_{11} + \kappa_{22}) \tag{57}$$

Hence the sensitivity of the maximum SIF with respect to the thickness is:

$$\begin{aligned}
K_{I,h}^{max} &= \left(\frac{1}{h}K_{1\ m,h} + \frac{6}{h^2}K_{1b,h} - \frac{1}{h^2}K_{1m} - \frac{12}{h^3}K_{1b}\right)T_\kappa \\
&+ \left(\frac{1}{h}K_{1m} + \frac{6}{h^2}K_{1b}\right)T_{\kappa,h} \\
K_{II,h}^{max} &= \left(\frac{1}{h}K_{2\ m,h} + \frac{6}{h^2}K_{2b,h} - \frac{1}{h^2}K_{2m} - \frac{12}{h^3}K_{2b}\right)T_\kappa \\
&+ \left(\frac{1}{h}K_{2m} + \frac{6}{h^2}K_{2b}\right)T_{\kappa,h} \\
K_{III,h}^{max} &= \left(\frac{3}{2h}K_{3b,h} - \frac{3}{2h^2}K_{3b}\right)T_\kappa + \left(\frac{3}{2h}K_{3b}\right)T_{\kappa,h}
\end{aligned} \tag{58}$$

where $()_{,h}$ represents the derivatives with respect to the thickness h. Once the sensitivities of the individual SIFs are obtained, the evaluation of the K_{eff} can be performed using the same equations given in Eqs. (28) and (35).

References

[1] H.O. Madsen, S. Krenk, N.C. Lind, Methods of Structural Safety, Dover Publications, 2006.

[2] A. Ghaderi, E. Ghavanloo, S.A. Fazelzadeh, Reliability analysis of carbon nanotube-based nano-truss under various loading conditions, Iran. J. Sci. Technol., Trans. Mech. Eng. 45 (2021) 1123–1131, http://dx.doi.org/10.1007/s40997-019-00340-w.

[3] B. Keshtegar, M.E. Amine, S. Zhu, R. Abbassi, N. Trung, Reliability analysis of corroded pipelines: Novel adaptive conjugate first order reliability method, J. Loss Prev. Process Ind. 62 (2021) 103986, http://dx.doi.org/10.1016/j.jlp.2019.103986.

[4] M.S. Chowdhury, C. Song, W. Gao, C. Wang, Reliability analysis of homogeneous and bimaterial cracked structures by the scaled boundary finite element method and a hybrid random-interval model, Struct. Saf. 59 (2016) 53–66, http://dx.doi.org/10.1016/j.strusafe.2015.11.003.

[5] X. Yuan, J. Gu, S. Liu, Sensitivity of sample for simulation-based reliability analysis methods, CMES Comput. Model. Eng. Sci. 126 (1) (2021) 331–357, http://dx.doi.org/10.32604/cmes.2021.010482.

[6] B.Q. Li, D.G. Lu, Comparisons of three meta-models for structural reliability analysis: RSM, ANN and SVR, in: 55th AIAA Structures, Structural Dynamics, and Materials Conference, 2013.

[7] C.H. Lee, Y. Kim, Probabilistic flaw assessment of a surface crack in a mooring chain using the first- and second-order reliability method, Mar. Struct. 63 (2019) 1–15, http://dx.doi.org/10.1016/j.marstruc.2018.09.003.

[8] L. Morse, Z. Sharif Khodaei, M.H. Aliabadi, A multi-fidelity boundary element method for structural reliability analysis with higher-order sensitivities, Eng. Anal. Bound. Elem. 104 (2019) 183–196, http://dx.doi.org/10.1016/j.enganabound.2019.03.036.

[9] T. Liu, F. Aldakheel, M.H. Aliabadi, Virtual element method for phase field modeling of dynamic fracture, Comput. Methods Appl. Mech. Engrg. 411 (2023) 116050, http://dx.doi.org/10.1016/j.cma.2023.116050.

[10] T. Liu, F. Aldakheel, M.H. Aliabadi, Hydrogen assisted cracking using an efficient virtual element scheme, Comput. Methods Appl. Mech. Engrg. (ISSN: 0045-7825) 420 (2024) 116708, http://dx.doi.org/10.1016/j.cma.2023.116708, URL https://www.sciencedirect.com/science/article/pii/S0045782523008319.

[11] Steven L. Crouch, Solution of plane elasticity problems by the displacement discontinuity method. I. Infinite body solution, Internat. J. Numer. Methods Engrg. 10 (1976) 301–343, URL https://api.semanticscholar.org/CorpusID:122865053.

[12] Steven L. Crouch, A.M. Starfield, Frank Rizzo, Boundary element methods in solid mechanics, 1983, URL https://api.semanticscholar.org/CorpusID:129858826.

[13] P. Partheymüller, M. Haas, G. Kuhn, Comparison of the basic and the discontinuity formulation of the 3D-dual boundary-element method, Eng. Anal. Bound. Elem. (ISSN: 0955-7997) 24 (10) (2000) 777–788, http://dx.doi.org/10.1016/S0955-7997(00)00060-6, URL https://www.sciencedirect.com/science/article/pii/S0955799700000606.

[14] John Weaver, Three-dimensional crack analysis, Int. J. Solids Struct. (ISSN: 0020-7683) 13 (4) (1977) 321–330, http://dx.doi.org/10.1016/0020-7683(77)90016-6, URL https://www.sciencedirect.com/science/article/pii/0020768377900166.

[15] M.H. Aliabadi, The Boundary Element Method: Applications in Solids and Structures, Vol. 2, John Wiley and Sons, 2002.

[16] A. Portela, M.H. Aliabadi, D.P. Rooke, The dual boundary element method: Effective implementation for crack problems, Internat. J. Numer. Methods Engrg. 33 (6) (1992) 1269–1287, http://dx.doi.org/10.1002/nme.1620330611.

[17] T. Dirgantara, M.H. Aliabadi, Dual boundary element formulation for fracture mechanics analysis of shear deformable shells, Int. J. Solids Struct. 38 (44) (2001) 7769–7800, http://dx.doi.org/10.1016/S0020-7683(01)00097-X.

[18] T. Dirgantara, M.H. Aliabadi, A new boundary element formulation for shear deformable shells analysis, Internat. J. Numer. Methods Engrg. 45 (9) (1999) 1257–1275, http://dx.doi.org/10.1002/(SICI)1097-0207(19990730)45:9<1257::AID-NME629>3.0.CO;2-N.

[19] V.V. Novozhilov, The Theory of Thin Elastic Shells, P. Noordhoff Ltd, Groningen, 1964.

[20] E. Reissner, Stress strain relations in the theory of thin elastic shells, J. Math. Phys. 31 (1952) 109–119, http://dx.doi.org/10.1002/sapm1952311109.

[21] P. Wen, M.H. Aliabadi, A. Young, Transformation of domain integrals to boundary integrals in BEM analysis of shear deformable plate bending problems, Comput. Mech. 24 (1999) 304–309, http://dx.doi.org/10.1007/s004660050519.

[22] C. Di Pisa, M.H. Aliabadi, Fatigue crack growth analysis of assembled plate structures with dual boundary element method, Eng. Fract. Mech. 98 (2013) 200–213, http://dx.doi.org/10.1016/j.engfracmech.2012.09.032.

[23] P.M. Baiz, M.H. Aliabadi, Buckling analysis of shear deformable shallow shells by the boundary element method, Eng. Anal. Bound. Elem. 31 (4) (2007) 361–372, http://dx.doi.org/10.1016/j.enganabound.2006.07.008.

[24] E.L. Albuquerque, M.H. Aliabadi, A boundary element analysis of symmetric laminated composite shallow shells, Comput. Methods Appl. Mech. Engrg. 199 (41) (2010) 2663–2668, http://dx.doi.org/10.1016/j.cma.2010.05.006.

[25] Brizeida Gámez, Eduardo Divo, Alain Kassab, Miguel Cerrolaza, Evaluation of fatigue crack growing in cortical bone using the BEM, Int. J. Healthc. Technol. Manag. 11 (2010) http://dx.doi.org/10.1504/IJHTM.2010.034090.

[26] T. Dirgantara, M.H. Aliabadi, Numerical simulation of fatigue crack growth in pressurized shells, Int. J. Fatigue 24 (7) (2002) 725–738, http://dx.doi.org/10.1016/S0142-1123(01)00195-5.

[27] J. Li, Z. Sharif Khodaei, M.H. Aliabadi, Dynamic fracture analysis of Kane–Mindlin plates using the dual boundary element method, Eng. Anal. Bound. Elem. 106 (2019) 217–227, http://dx.doi.org/10.1016/j.enganabound.2019.05.005.

[28] J. Useche, Fracture dynamic analysis of cracked Reissner plates using the boundary element method, Int. J. Solids Struct. 191–192 (2020) 315–332, http://dx.doi.org/10.1016/j.ijsolstr.2020.01.017.

[29] R. Masoudi Nejad, Z. Liu, W. Ma, F. Berto, Fatigue reliability assessment of a pearlitic Grade 900 A rail steel subjected to multiple cracks, Eng. Fail. Anal. (ISSN: 1350-6307) 128 (2021) 105625, http://dx.doi.org/10.1016/j.engfailanal.2021.105625.

[30] P. Ni, J. Li, H. Hao, W. Yan, X. Du, H. Zhou, Reliability analysis and design optimization of nonlinear structures, Reliab. Eng. Syst. Saf. (ISSN: 0951-8320) 198 (2020) 106860, http://dx.doi.org/10.1016/j.ress.2020.106860.

[31] R. Teixeira, M. Nogal, A. O'Connor, Adaptive approaches in metamodel-based reliability analysis: A review, Struct. Saf. (ISSN: 0167-4730) 89 (2021) 102019, http://dx.doi.org/10.1016/j.strusafe.2020.102019.

[32] L. Morse, Z. Sharif Khodaei, M.H. Aliabadi, Multi-fidelity modeling-based structural reliability analysis with the boundary element method, J. Multiscale Model. 08 (2017) 1740001, http://dx.doi.org/10.1142/S1756973717400017.

[33] X. Huang, M.H. Aliabadi, A boundary element method for structural reliability, Key Eng. Mater. 627 (2015) 453–456, http://dx.doi.org/10.4028/www.scientific.net/KEM.627.453.

[34] C. Su, J. Xu, Reliability analysis of Reissner plate bending problems by stochastic spline fictitious boundary element method, Eng. Anal. Bound. Elem. 51 (2015) 37–43, http://dx.doi.org/10.1016/j.enganabound.2014.10.006.

[35] L. Morse, Z. Sharif Khodaei, M.H. Aliabadi, A dual boundary element based implicit differentiation method for determining stress intensity factor sensitivities for plate bending problems, Eng. Anal. Bound. Elem. 106 (2019) 412–426, http://dx.doi.org/10.1016/j.enganabound.2019.05.021.

[36] R. Masoudi Nejad, Z. Liu, W. Ma, F. Berto, Reliability analysis of fatigue crack growth for rail steel under variable amplitude service loading conditions and wear, Int. J. Fatigue 152 (2021) 106450, http://dx.doi.org/10.1016/j.ijfatigue.2021.106450.

[37] X. Huang, M.H. Aliabadi, Z. Sharif Khodaei, Fatigue crack growth reliability analysis by stochastic boundary element method, CMES Comput. Model. Eng. Sci. 102 (4) (2014) 291–330, http://dx.doi.org/10.3970/cmes.2014.102.291.

[38] E. Leonel, A. Chateauneuf, W. Venturini, Probabilistic crack growth analyses using a boundary element model: Applications in linear elastic fracture and fatigue problems, Eng. Anal. Bound. Elem. 36 (2012) 944–959, http://dx.doi.org/10.1016/j.enganabound.2011.12.016.

[39] M. Zhuang, L. Morse, Z. Sharif Khodaei, M.H. Aliabadi, Implicit differentiation-based reliability analysis for shallow shell structures with the Boundary Element Method, Eng. Anal. Bound. Elem. 156 (2023) 223–238, http://dx.doi.org/10.1016/j.enganabound.2023.07.041.

[40] T. Dirgantara, M.H. Aliabadi, Stress intensity factors for cracks in thin plates, Eng. Fract. Mech. (ISSN: 0013-7944) 69 (13) (2002) 1465–1486, http://dx.doi.org/10.1016/S0013-7944(01)00136-9, URL https://www.sciencedirect.com/science/article/pii/S0013794401001369.

[41] Measures of structural reliability, in: Structural Reliability Analysis and Prediction, John Wiley & Sons, Ltd, ISBN: 9781119266105, 2017, pp. 1–29, http://dx.doi.org/10.1002/9781119266105.ch1.

[42] G. Jia, X. Du, Reliability sensitivity analysis with random and interval variables, Internat. J. Numer. Methods Engrg. 78 (13) (2009) 1585–1617, http://dx.doi.org/10.1002/nme.2543.

[43] S. Abdullah, S. Beden, A.K. Ariffin, Fatigue crack growth simulation of aluminium alloy under cyclic sequence effects, 2011, http://dx.doi.org/10.5772/14898.

[44] P. Lopes, H. Gomes, A.M. Awruch, Reliability analysis of laminated composite structures using finite elements and neural networks, Compos. Struct. 92 (2010) 1603–1613, http://dx.doi.org/10.1016/j.compstruct.2009.11.023.

[45] H. Tang, X. Guo, S. Xue, Uncertainty quantification in small-timescale model-based fatigue crack growth analysis using a stochastic collocation method, Metals (ISSN: 2075-4701) 10 (5) (2020) http://dx.doi.org/10.3390/met10050646.

[46] Pengpeng Zhi, Yonghua Li, Bingzhi Chen, Shanshan Shi, Bounds-based structure reliability analysis of bogie frame under variable load cases, Eng. Fail. Anal. (ISSN: 1350-6307) 114 (2020) 104541, http://dx.doi.org/10.1016/j.engfailanal.2020.104541, URL https://www.sciencedirect.com/science/article/pii/S1350630719319892.

[47] Ning Li, De-Quan Zhang, Hai-Tao Liu, Tie-Jun Li, Optimal design and strength reliability analysis of pressure shell with grid sandwich structure, Ocean Eng. (ISSN: 0029-8018) 223 (2021) 108657, http://dx.doi.org/10.1016/j.oceaneng.2021.108657, URL https://www.sciencedirect.com/science/article/pii/S0029801821000925.

[48] Ouk Lee, Dong Kim, Reliability of Fatigue Damaged Structure Using FORM, SORM and Fatigue Model, in: Lecture Notes in Engineering and Computer Science, Vol. 2166, 2007.

[49] Masoud Rais-Rohani, Reliability Analysis and Reliability-Based Design Optimization of Circular Composite Cylinders under Axial Compression, NASA Langley Research Center, 2000.

[50] V. Dubourg, J.-M. Bourinet, B. Sudret, Reliability-based design optimization of shells with uncertain geometry using adaptive Kriging metamodels, 2017, URL https://www.academia.edu/33301072/RELIABILITY_BASED_DESIGN_OPTIMIZATION_OF_SHELLS_WITH_UNCERTAIN_GEOMETRY_USING_ADAPTIVE_KRIGING.

[51] H.O. Madsen, Methods of Structural Safety, Dover ed., Dover Publications, Mineola, NY, 2006-1986.

[52] Peyman Amirafshari, Feargal Brennan, Athanasios Kolios, A fracture mechanics framework for optimising design and inspection of offshore wind turbine support structures against fatigue failure, Wind Energy Sci. 6 (2021) 677–699, http://dx.doi.org/10.5194/wes-6-677-2021.

[53] G. Georgiou, PoD curves, their derivation, applications and limitations, Insight 49 (2007) 409–414, http://dx.doi.org/10.1784/insi.2007.49.7.409.

[54] Henrik O. Madsen, Omission sensitivity factors, Struct. Saf. (ISSN: 0167-4730) 5 (1) (1988) 35–45, http://dx.doi.org/10.1016/0167-4730(88)90004-5, URL https://www.sciencedirect.com/science/article/pii/0167473088900045.